Monthly Notices of the ROYAL ASTRONOMICAL SOCIETY

MNRAS **539,** 2362–2379 (2025) https://doi.org/10.1093/mnras/staf613
Advance Access publication 2025 April 12

On the relationship between the cosmic web and the alignment of galaxies and AGN jets

S. Lyla Jung [1]★ I. H. Whittam [1] M. J. Jarvis [1,2] C. L. Hale [1] M. N. Tudorache [1] and T. Yasin [1]

[1]*Sub-department of Astrophysics, Department of Physics, University of Oxford, Denys Wilkinson Building, Keble Road, Oxford OX1 3RH, UK*
[2]*Department of Physics and Astronomy, University of the Western Cape, Robert Sobukwe Road, 7535 Bellville, Cape Town, South Africa*

Accepted 2025 April 10. Received 2025 April 4; in original form 2025 February 5

ABSTRACT

The impact of active galactic nuclei (AGNs) on the evolution of galaxies explains the steep decrease in the number density of the most massive galaxies in the Universe. However, the fuelling of the AGN and the efficiency of this feedback largely depend on their environment. We use data from the Low Frequency Array Two-metre Sky Survey Data Release 2 (DR2), the Dark Energy Spectroscopic Instrument Legacy Imaging Surveys, and the Sloan Digital Sky Survey DR12 to make the first study of the orientations of radio jets and their optical counterpart in relation to the cosmic web environment. We find that close to filaments ($\lesssim$11 Mpc), galaxies tend to have their optical major axes aligned with the nearest filaments. On the other hand, radio jets, which are generally aligned perpendicularly to the optical major axis of the host galaxy, show more randomized orientations with respect to host galaxies within $\lesssim$8 Mpc of filaments. These results support the scenario that massive galaxies in cosmic filaments grow by numerous mergers directed along the orientation of the filaments while experiencing chaotic accretion of gas on to the central black hole. The AGN-driven jets consequently have a strong impact preferentially along the minor axes of dark matter haloes within filaments. We discuss the implications of these results for large-scale radio jet alignments, intrinsic alignments between galaxies, and the azimuthal anisotropy of the distribution of circumgalactic medium and anisotropic quenching.

Key words: methods: observational – galaxies: evolution – galaxies: jets – large-scale structure of Universe.

1 INTRODUCTION

It has long been established that supermassive black holes (SMBHs) reside at the core of possibly all massive galaxies (Kormendy & Richstone 1995). As the strong gravity field around an SMBH accretes surrounding interstellar material on to the black hole, large amounts of energy can be released producing active galactic nucleus (AGN) activity. It is thought that AGN accretion occurs in two different modes, resulting in two different classes of AGNs. The first is 'jet mode' AGN, which accretes inefficiently from pockets of cold gas in the hot gas halo and emits the bulk of its power as a radio jet. The second are the radiatively efficient 'radiative mode' sources typical of optical or X-ray-selected AGN, which accretes efficiently from cold gas and may or may not have a radio jet (e.g. Heckman & Best 2014).

Galaxy formation models invoke feedback from such AGN to curtail the amount of star formation in massive galaxies and match the observed galaxy stellar mass function (e.g. Bower et al. 2006, 2017; Croton et al. 2006; Adams et al. 2021; McLeod et al. 2021; Jung et al. 2022). This feedback is often prescribed as two related processes that are implemented in recent cosmological-volume galaxy formation simulations, albeit with slightly different prescriptions (e.g. Schaye et al. 2015; Dubois et al. 2016; Davé et al. 2019). First, the radiative feedback from the hard ionization field emanating from the accretion disc provides a heating mechanism for the surrounding gas, preventing it from cooling and condensing into cold gas necessary for star formation; the second mechanism arises from the generation of jet outflows, which can drive gas away from the host galaxy via mechanical feedback (e.g. Heckman et al. 2024). These AGN jets may also have an impact on galaxy groups and clusters (e.g. Fabian 2012; McNamara & Nulsen 2012) potentially stimulating or truncating star formation within galaxies in such environments (Rawlings & Jarvis 2004; Hatch et al. 2014).

However, such a clear distinction between 'radiative' and 'mechanical' feedback modes is possibly not completely correct. Many AGNs that have both bright optical nuclei and broad-line regions, which are the hallmark of the radiative mode, also produce powerful radio emission, traditionally termed radio-loud quasars and radio galaxies (see Urry & Padovani 1995, for a review). Furthermore, although large samples of bright radio sources tend to exhibit a bimodal distribution in their Eddington-scaled accretion rate (Best & Heckman 2012; Mingo et al. 2014), more recent work using deeper radio data suggests that this bimodal distribution disappears towards lower radio luminosities (Whittam et al. 2018, 2022). The relationship between the accretion rate and the generation of jets responsible for the mechanical feedback in these systems is therefore a critical aspect in enhancing our understanding of the role of AGN in galaxy evolution.

Theoretical models of AGN jet formation suggest that the jets are launched along the axis of the black hole spin. If the gas accretion on to the black hole has a preferred direction with respect to an AGN host galaxy, this may result in a preferred orientation for jets. The direction of radio jets with respect to their host galaxies has

★ E-mail: lyla.jung@physics.ox.ac.uk

been explored observationally by comparing the position angles of extended radio sources and their optical counterparts. Although early studies reported mixed views on alignment (Mackay 1971; Palimaka et al. 1979; Valtonen 1983; Birkinshaw & Davies 1985; Sansom et al. 1987), recent investigations based on large statistical samples suggest that radio jets tend to align with the optical minor axis on both the kpc scale (Battye & Browne 2009; Zheng, Zhang & Röttgering 2024) and the pc scale (Fernández Gil et al. 2024). Of particular relevance to this paper, Zheng et al. (2024) analyse radio sources from the Low Frequency Array (LOFAR) Two-metre Sky Survey Data Release 2 (LoTSS DR2; Shimwell et al. 2022) and show that the tendency for the jet–galaxy alignment depends on various properties such as the radio luminosity, the physical size of jets, the stellar mass, and the shape of host galaxies. This finding indicates that how the jets are launched and propagated is closely linked with the evolution of their host galaxies.

At a larger intergalactic scale, a relevant yet inconclusive question is whether there is a specific angular scale or regions in the sky in which the orientations of adjacent radio jets are coherent. If such coherency is indeed present, it implies that the spin axes of black holes are aligned over several tens of Mpc and larger physical scales, which can be attributed to the large-scale structure of the Universe. Some studies support the large-scale alignment of jets at several to tens of degrees scales (Taylor & Jagannathan 2016; Contigiani et al. 2017; Panwar et al. 2020; Mandarakas et al. 2021). However, more recent investigations do not support a statistically significant correlation among adjacent radio galaxies in the 3D space identified using photometric or spectroscopic redshifts (Osinga et al. 2020; Simonte et al. 2023). The link between the large-scale intergalactic environment and radio jets therefore remains unclear.

The influence of the large-scale cosmic web environment on galaxy evolution appears to be more clearly reflected in the shape and kinematic properties of galaxies (e.g. Zhang et al. 2015; Hirv et al. 2017; Kraljic et al. 2021; Barsanti et al. 2022, 2023; Tudorache et al. 2022; Lee & Moon 2023). Numerical simulations of cosmological structure formation demonstrate that as the universe evolves, galaxies and dark matter haloes in filaments migrate towards denser nodes where galaxy groups and clusters develop (e.g. Springel et al. 2005). Some of these galaxies and haloes undergo mergers that predominantly occur along the direction of the filament they reside in (Libeskind et al. 2014; Kang & Wang 2015). As a result, these simulations predict that massive galaxies in cosmic filaments tend to elongate along the filaments and have angular momentum perpendicular to the filament direction (Aragón-Calvo et al. 2007; Codis et al. 2012; Libeskind et al. 2013; Dubois et al. 2014; Wang & Kang 2017).

Observationally, Tempel & Libeskind (2013) report that elliptical galaxies in the Sloan Digital Sky Survey (SDSS) DR8 spectroscopic galaxy sample (Aihara et al. 2011; Tempel, Tago & Liivamägi 2012) preferentially have the optical minor axes perpendicular to the nearest cosmic filaments. On the other hand, lower mass galaxies tend to have their spin axes aligned with the filaments (e.g. Kraljic et al. 2021; Tudorache et al. 2022). Such a non-negligible correlation between galaxy shape and cosmic filaments provides a physical basis for the intrinsic alignment among galaxies over large angular scales that affects the interpretation of weak-gravitational lensing-based cosmic shear measurements (Hirata et al. 2007; Joachimi et al. 2011; Chisari et al. 2015; Singh, Mandelbaum & More 2015).

In this paper, we explore the alignments between optical galaxies, radio jets, and cosmic filaments. Specifically, we focus on how the galaxy–filament and galaxy–jet alignments vary according to the cosmic web environment. The paper is structured as follows. Section 2 gives an overview of the data used in this study and explains how we define our samples. We present our analysis of the alignment between optical galaxies and cosmic filaments in Section 3.1. The analysis of the alignment between optical galaxies and radio jets is presented in Section 3.2. In Sections 4.1 and 4.2, we discuss the physical mechanisms and implications of our findings. Section 5 is the summary of this paper. Throughout the paper, we assume a Lambda cold dark matter cosmology based on Planck Collaboration XIII (2016) results: $\Omega_{\rm m} = 0.309$, $\Omega_\Lambda = 0.691$, $\Omega_{\rm b} = 0.0486$, $H_0 = 67.8\,{\rm km\,s^{-1}\,Mpc^{-1}}$, and $\sigma_8 = 0.82$.

2 DATA

In this study, we compile a radio galaxy sample and their host galaxy properties and cosmic environments from several multiwavelength surveys. In Section 2.1, we provide a brief overview of LoTSS DR2 (Shimwell et al. 2022) and the radio-optical/infrared cross-match catalogue of LoTSS DR2 sources (Hardcastle et al. 2023). Section 2.2 describes the Dark Energy Spectroscopic Instrument (DESI) Legacy Imaging Surveys (Dey et al. 2019) where we retrieve optical properties of our radio galaxy sample. For characterizing the cosmic environment, we use the cosmic filament catalogue published by Malavasi et al. (2020), which will be explained in Section 2.3. We describe the galaxy samples used in this study in Section 2.4.

2.1 LoTSS DR2 and the optical value-added catalogue

LoTSS DR2 covers 27 per cent of the northern sky ($\sim$5700 deg^2), split into two continuous fields, RA-1 and RA-13 centred at (RA, Dec.) = ($1^{\rm h}00^{\rm m}00^{\rm s}$, $+28^\circ00'00''$) and ($12^{\rm h}45^{\rm m}00^{\rm s}$, $+44^\circ30'00''$), respectively. LoTSS DR2 observes the sky using LOFAR's (van Haarlem et al. 2013) high-band antennas, operating at 120–168 MHz. In total, about 4 million radio sources were identified throughout the fields using the Python Blob Detector and Source Finder (PYBDSF; Mohan & Rafferty 2015).

The cross-matching between the radio and optical/infrared sources was carried out by Hardcastle et al. (2023) using a combination of a likelihood-ratio method (Sutherland & Saunders 1992; McAlpine et al. 2012) and visual inspection by citizen scientists via the Zooniverse project, 'Radio Galaxy Zoo: LOFAR',[1] hereafter, RGZ(L). This strategy is similar to that described in Williams et al. (2019); however, notably, Hardcastle et al. (2023) restricted the sources that could go through the Galaxy Zoo process to those sources $\geq$4 mJy. This was due to the increased area of LoTSS DR2 compared to DR1 (>10 times of Shimwell et al. 2019) leading to a significant increase in sources. Accurate positional information is crucial for William Herschel Telescope Enhanced Area Velocity Explorer-LOFAR (WEAVE-LOFAR; Smith et al. 2016), for which the wide-area survey has a minimum flux density limit of 8 mJy. Therefore, 4 mJy was used so that multicomponent sources whose total flux density would sum to 8 mJy could be identified and cross-matched together. This radio-optical cross-matched catalogue provides key parameters for this study, including the redshift and stellar mass of optical galaxies hosting the radio sources. For reference, of the 4 million radio sources in the catalogue, about 60 per cent (50 per cent) have redshift (stellar mass) measurements.

One of the key radio properties investigated in this study is the position angle of extended radio jets. We provide more details of how we identified the sample with extended radio jets in Section 2.4.

[1] http://lofargalaxyzoo.nl/

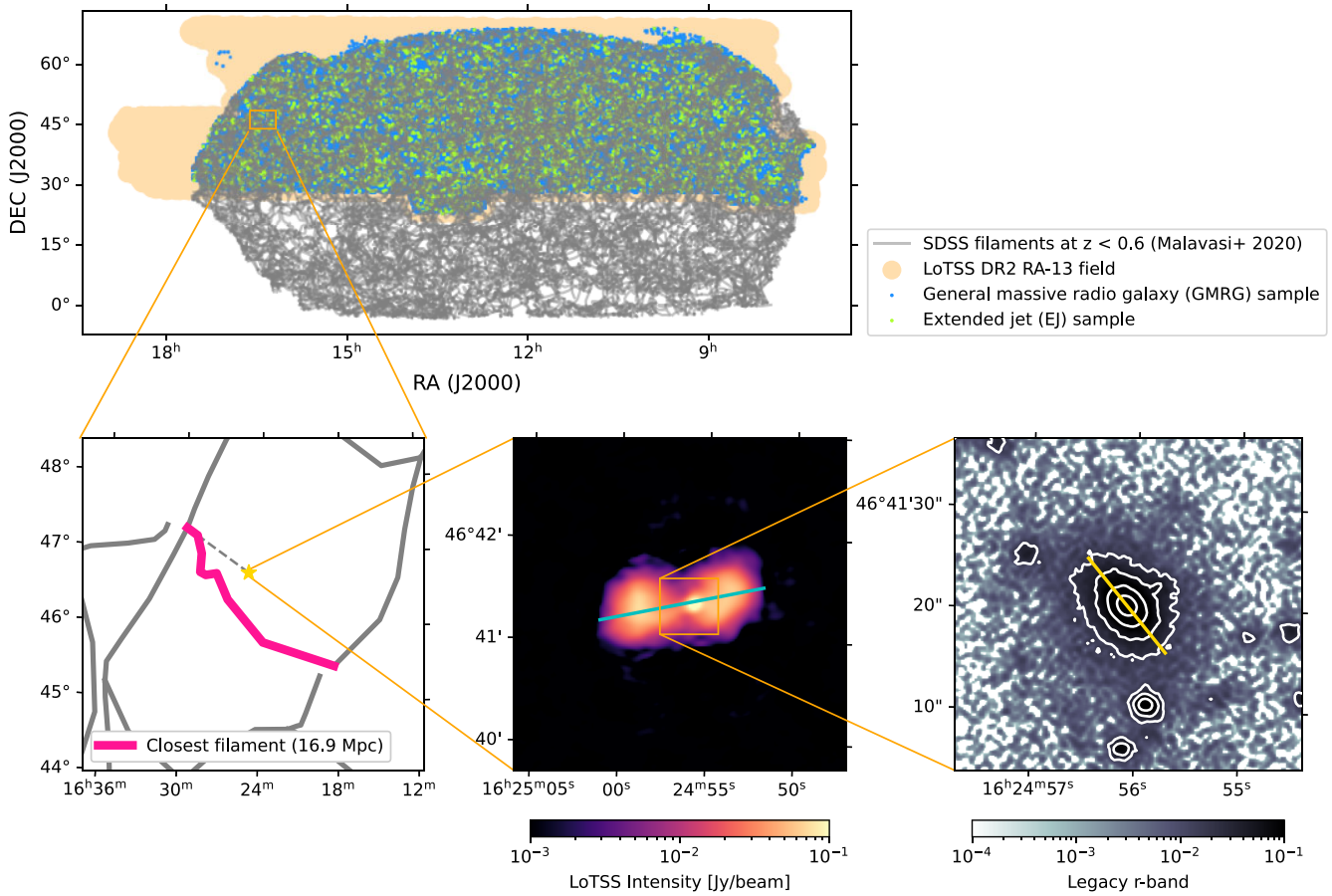

Figure 1. Top panel: The sky coverage of different data used in this study. The grey lines are cosmic filaments below redshift of 0.6 catalogued by Malavasi et al. (2020). The peach-coloured shade shows the RA-13 field of LoTSS DR2. The GMRG and the EJ samples defined in Section 2.4 are shown with the blue and the green dots, respectively. Bottom panels: We randomly select a galaxy in the EJ sample and show the surrounding cosmic filament distribution (left panel), the radio image (middle panel), and the r-band image (right panel). The filament closest to the example source, the radio major axis, and the optical major axis are shown in coloured lines (pink, blue, and yellow, respectively). The distance between the closest filament and the source is 16.9 Mpc, as indicated in the legend in the left panel.

Here, we explain how the position angle of radio sources is defined depending on the source structure ('S_Code').

PYBDSF classifies the radio sources into three categories depending on the source structure. 'S' sources are isolated and fitted by a single Gaussian. 'C' sources are fitted by a single Gaussian and located within a group of emissions (i.e. an island) containing other sources. 'M' sources are fitted with multiple Gaussians. The 'S_Code' column in the cross-matched catalogue contains information about this PYBDSF source category or an additional category 'Z' for sources identified as a composite source in the RGZ(L) where multiple PYBDSF sources needed associating together into a single object.

For 'S'- and 'M'-type sources, we use the deconvolved position angle identified by PYBDSF (the 'DC_PA' column in the cross-matched catalogue). This is the angle of the source's major axis identified using image moment analysis.[2] Note that all position angles in this study are measured east of north. For 'Z'-type composite sources, the position angle is determined as the angle of the longest axis of a convex hull enclosing all components of a source (the 'Composite_PA' column in the cross-matched catalogue). For example, the bottom middle panel in Fig. 1 shows a LoTSS image of a randomly selected radio source from the extended jet (EJ) sample that we define shortly. The major axis of the source is shown in a blue straight line. The position angle of this source is 101°.

The RGZ(L) provides a supplementary catalogue of tags assigned by volunteers (for example, see table 3 of Hardcastle et al. 2023). These tags include descriptions of morphologies of radio sources, such as 'nat' (narrow angle tail), 'wat' (wide angle tail), 'bent', 'blend', 'x-shaped', 's-shaped', and 'v-shaped'.

2.2 DESI Legacy Imaging Surveys

While the LoTSS DR2 radio-optical cross-matching catalogue includes basic properties of radio galaxy hosts (e.g. coordinate, redshift, and g-, r-, and z-band magnitudes), we revisit the 'sweep' catalogues of the DESI Legacy Imaging Surveys (Dey et al. 2019) to obtain further information about the optical sources matched with the LoTSS radio sources. For this task, we use the 'RELEASE', 'BRICKID', and 'OBJID' fields in the LoTSS catalogue, indicating the Legacy release number, brick ID, and object ID, respectively. All matched optical sources are from the Legacy Surveys DR8. At declination $\delta > +32.^{\circ}375$, the Legacy catalogue includes sources from the Beijing-Arizona Sky Survey (BASS; Zou et al. 2017) and the Mayall z-band Legacy Survey (MzLS). At lower declinations,

[2] https://pybdsf.readthedocs.io/en/latest/algorithms.html#grouping-of-gaussians-into-sources

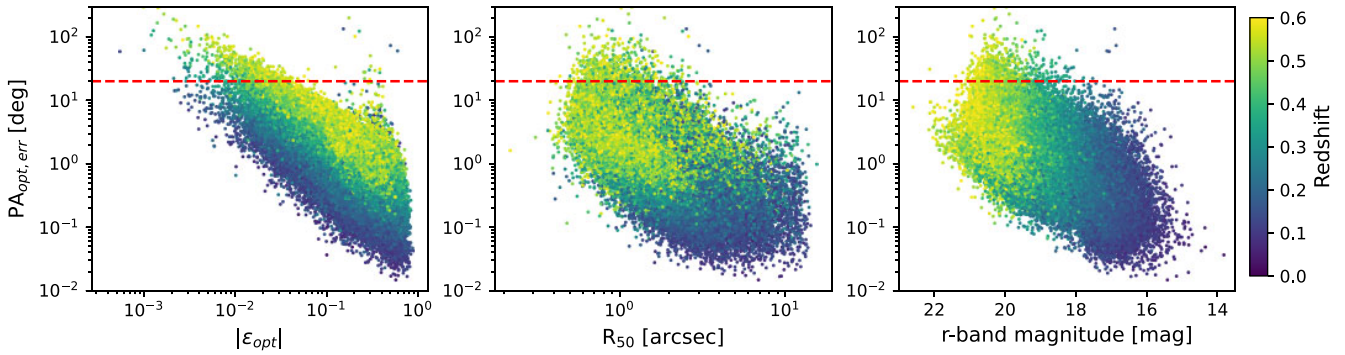

Figure 2. The uncertainty of the optical position angles ($PA_{opt,err}$) as a function of optical ellipticity ($|\epsilon_{opt}|$, left panel), optical half-light radius (R_{50}, middle panel), r-band magnitude (right panel), and redshift (colour of points in all panels). The horizontal dashed line shows the 20° limit we apply to remove galaxies with high uncertainties.

sources are taken from the Dark Energy Camera (DECam) Legacy Survey (DECaLS).

The Legacy Surveys perform photometry using the TRACTOR algorithm (Lang, Hogg & Schlegel 2016). In this framework, sources are classified into different types depending on the best-fitting morphological model (the 'type' column in the DESI Legacy catalogue). As we are interested in measuring the position angle of optical galaxies, types relevant to our analysis are spatially extended sources with a meaningful position angle: 'EXP', 'DEV', and 'COMP'. These types indicate that the isophots of sources are best modelled with the exponential profile ('EXP'), deVaucouleurs profile ('DEV'), and the composite profile (exponential plus deVaucouleurs; 'COMP'), respectively.

Some of the key fields in the DESI Legacy catalogue we use for this study are the ellipticities of the optical sources ('SHAPEEXP_E1', 'SHAPEEXP_E2', 'SHAPEDEV_E1', and 'SHAPEDEV_E2' columns). The optical ellipticity is defined as a complex number[3] using these fields:

$$\epsilon_{\rm opt} = \frac{a-b}{a+b}\exp(2{\rm i}\,{\rm PA}_{\rm opt}) = \epsilon_1 + {\rm i}\epsilon_2, \tag{1}$$

where a, b, and PA_{opt} are the major and minor axes and the position angle of the ellipse fitted to the isophotes. Here, ϵ_1 and ϵ_2 are the two ellipticities given by the catalogue, each labelled with '_E1' and '_E2' in the columns. The above equation can be rearranged as

$$\mathrm{PA}_{\rm opt} = \begin{cases} \frac{1}{2}\arctan\left(\frac{\epsilon_2}{\epsilon_1}\right) & \text{if } \epsilon_1 > 0, \\ \frac{1}{2}\arctan\left(\frac{\epsilon_2}{\epsilon_1}\right) + \frac{\pi}{2} & \text{if } \epsilon_1 < 0 \text{ and } \epsilon_2 > 0, \\ \frac{1}{2}\arctan\left(\frac{\epsilon_2}{\epsilon_1}\right) - \frac{\pi}{2} & \text{if } \epsilon_1 < 0 \text{ and } \epsilon_2 < 0, \\ +\frac{\pi}{4} & \text{if } \epsilon_1 = 0 \text{ and } \epsilon_2 > 0, \\ -\frac{\pi}{4} & \text{if } \epsilon_1 = 0 \text{ and } \epsilon_2 < 0, \\ \text{Undefined} & \text{if } \epsilon_1 = 0 \text{ and } \epsilon_2 = 0. \end{cases} \tag{2}$$

For 'EXP'- and 'DEV'-type sources, the ellipticities ϵ_1 and ϵ_2, and therefore PA_{opt}, are only defined for the best-fitting model, either exponential or deVaucouleurs. For 'COMP'-type sources, ellipticities are given separately for the exponential and deVaucouleurs components of the composite fit (labelled with 'SHAPEEXP' and 'SHAPEDEV' in the columns). We confirm that $\lesssim$4 per cent of our sample falls into this case. For these galaxies, we calculate the position angle of each component separately and take the average value as the representative PA_{opt} of the source.

As the DESI Legacy catalogue provides uncertainties of ϵ_1 and ϵ_2, we calculate the uncertainty of the optical position angles by propagating the uncertainties as

$$\mathrm{PA}_{\rm opt,err} = \frac{1}{2}\frac{\sqrt{\epsilon_2^2\sigma_{\epsilon_1}^2 + \epsilon_1^2\sigma_{\epsilon_2}^2}}{\epsilon_1^2+\epsilon_2^2}, \tag{3}$$

where $\sigma_{\epsilon_1}^2$ and $\sigma_{\epsilon_2}^2$ are the variance of ϵ_1 and ϵ_2, respectively, which can be obtained using the inverse variance of the ellipticities given in the catalogue (columns 'SHAPEEXP_E1_IVAR', 'SHAPEEXP_E2_IVAR', 'SHAPEDEV_E1_IVAR', and 'SHAPEDEV_E2_IVAR'). Fig. 2 shows the $PA_{opt,err}$ of galaxies for this study as a function of optical ellipticity (left panel), optical half-light radius (middle panel), r-band magnitude (right panel), and redshift (colour in all panels). We apply the upper limit on the optical position angle uncertainty ($PA_{opt,err} < 20°$, horizontal dashed line) to limit our analysis to galaxies with well-defined PA_{opt}. This criterion excludes galaxies that are too round, small, and faint to obtain a reliable optical position angle,[4] predominantly at high redshift. The bottom right panel in Fig. 1 shows the Legacy g-band cut-out image of the example source and its optical major axis (yellow line). The optical position angle of this source is 38.90° with an uncertainty of 0.25°.

For a subset of galaxies in the DESI Legacy Surveys, morphology information is provided by Galaxy Zoo DESI (Walmsley et al. 2023). Galaxy Zoo DESI combines visual inspections by volunteers with deep learning models to enable morphology measurements of the large data set. The Galaxy Zoo framework includes questions about whether there is a sign of ongoing mergers for a given galaxy and provides the fraction of volunteer votes. As PA_{opt} of galaxies with ongoing mergers are often ill-defined, we use $f_{\rm merging=none}$ parameter (i.e. the fraction of volunteer votes for the system not

[3]This definition is taken from a weak gravitational lensing formalism (e.g. Bridle et al. 2009). See https://www.legacysurvey.org/dr8/catalogs/.

[4]In Zheng et al. (2024), the authors adopt sample selection criteria based on the optical axis ratio ($b/a < 0.8$) and the optical radius ($R_{50} > 1.5$ arcsec) that explicitly remove round and small galaxies with potentially unreliable optical position angles. Although we do not implement the same criteria, we confirm that the results of this paper do not change when excluding low-ellipticity ($|\epsilon_{\rm opt}| < 0.1$), small galaxies ($R_{50} < 1.5$ arcsec) from the analysis.

showing any sign of mergers or tidal interactions; column 'merging_none_fraction') to identify merging galaxies ($f_{\rm merging=none} \leqslant 0.5$) and exclude them from the analysis presented in this paper. Note that this procedure only applies to bright galaxies (r-band magnitude <19) with the Galaxy Zoo DESI information available (<30 per cent of the total sample among which the merging fraction is ∼4 per cent). Therefore, the identification of merging systems may not be complete.

2.3 SDSS cosmic filaments

Malavasi et al. (2020) present catalogues of cosmic filaments identified by applying the Discrete Persistent Structure Extractor (DisPerSE; Sousbie 2011) algorithm to the SDSS galaxy distribution. In this study, we use a filament catalogue created using the SDSS DR12 (Alam et al. 2015) LOWZ + CMASS sample (see Reid et al. 2016 for the definition of the sample).This sample spans a broader redshift range ($z \approx 0$–0.8) compared to the other available option, i.e. SDSS DR7 main galaxy sample (Strauss et al. 2002), which covers $z \approx 0$–0.3. The large redshift coverage offers a large 3D volume of the Universe to study numerous cosmic filaments.

There are several input parameters incorporated into the DisPerSE filament-finding algorithm that could influence the overall properties (e.g. shape and length) of catalogued filaments: (i) the number of density field smoothing cycles, (ii) the persistence threshold, and (iii) the number of skeleton smoothing cycles. In short, smoothing the density field prior to the filament finding helps reduce noise in the galaxy distribution, which can otherwise result in unphysical structures. Increasing the persistence threshold effectively reduces the detection of less significant short branches of cosmic filaments. Smoothing of the skeletons removes any sharp edges of the identified filaments. See section 4 of Malavasi et al. (2020) for a detailed discussion on the choice of parameters. We use the catalogue with one cycle of density smoothing, the persistence threshold of 3σ, and one cycle of skeleton smoothing. The distribution of the filaments in the 2D sky plane is shown in the top panel of Fig. 1 with grey lines.

Each DisPerSE filament is composed of multiple sampling points. The filament catalogue provides the 3D coordinates (RA, Dec., redshift) of sampling points. For the purpose of this study, we identify the cosmic filament closest to each galaxy in our samples and measure the position angle of the matched filament segment. We use `astropy.coordinates.match_coordinates_3d` function to identify a filament sampling point closest to each LoTSS source with redshift measurements and measure the 3D distance between the matched filament and the source. In this process, all galaxy and filament coordinates are converted to Cartesian coordinates (x, y, z) using

$$\begin{aligned} x &= d\sin(\alpha)\cos(\beta), \\ y &= d\sin(\alpha)\sin(\beta), \\ z &= d\cos(\alpha), \end{aligned} \tag{4}$$

where $\alpha = \pi/2 - \mathrm{Dec.}$, $\beta = \mathrm{RA}$, and d is the distance to the filament sampling point calculated from its redshift. The average spacing between adjacent DisPerSE filament sampling points is small (≈14 Mpc) compared to the average distance between a galaxy and the closest filament (≈40 Mpc; see Section 2.4 for further discussion). The bottom left panel of Fig. 1 illustrates the cosmic filament distribution close to the example galaxy (star symbol) shown in the right panels. The closest filament is highlighted with a thick pink-coloured line, and the dashed line connects the galaxy and the closest filament sampling point. Note that we use the distance in the 3D coordinate system to identify the closest filament sampling point, not the angular separation.

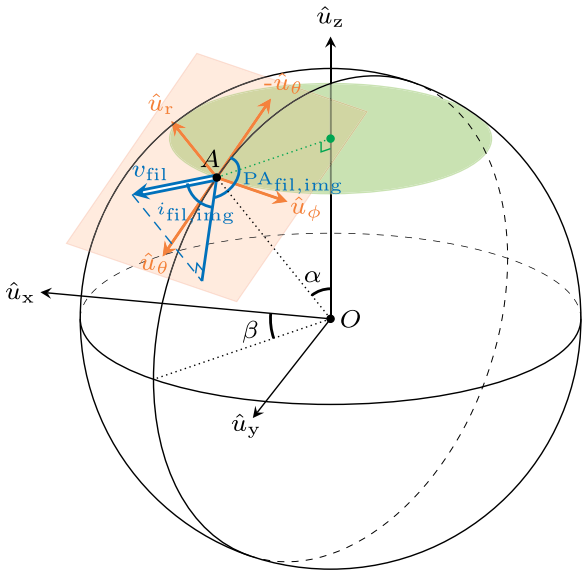

Figure 3. An illustration showing the Cartesian coordinate $(\hat{\boldsymbol{u}}_x, \hat{\boldsymbol{u}}_y, \hat{\boldsymbol{u}}_z)$ and the local spherical coordinate $(\hat{\boldsymbol{u}}_r, \hat{\boldsymbol{u}}_\theta, \hat{\boldsymbol{u}}_\phi)$ on the celestial sphere. The point A and the vector $\boldsymbol{v}_{\rm fil}$ represent the location of a filament sampling point and the filament orientation vector, respectively. We measure the inclination and the position angle of the filament at point A by transforming $\boldsymbol{v}_{\rm fil}$ from the Cartesian coordinate to the spherical coordinate. See Section 2.3 for further explanations.

Once the closest filament sampling point is identified, we define a filament orientation vector ($\boldsymbol{v}_{\rm fil}$) connecting the two adjacent sampling points of the same filament. If the closest sampling point is at the end of a filament, we use a vector connecting the closest point and the adjacent point of the same filament. As DisPerSE filaments are defined in the 3D space, this vector is also in the 3D Cartesian coordinate:

$$\boldsymbol{v}_{\rm fil} = v_x\hat{\boldsymbol{u}}_x + v_y\hat{\boldsymbol{u}}_y + v_z\hat{\boldsymbol{u}}_z, \tag{5}$$

where (v_x, v_y, v_z) are vector components in the Cartesian coordinate system with the basis of unit vectors $(\hat{\boldsymbol{u}}_x, \hat{\boldsymbol{u}}_y, \hat{\boldsymbol{u}}_z)$.

Fig. 3 illustrates how we convert a vector ($\boldsymbol{v}_{\rm fil}$) in the Cartesian coordinate to the local spherical coordinate with the basis of $(\hat{\boldsymbol{u}}_r, \hat{\boldsymbol{u}}_\theta, \hat{\boldsymbol{u}}_\phi)$ in order to measure the position angle and inclination of the vector. We set the location of a filament sampling point on the celestial sphere as A and show an arbitrary filament orientation vector at this location with a blue double arrow. We convert the vector to the local spherical coordinate system using the following relation (Lee & Erdogdu 2007):

$$\begin{bmatrix} v_r \\ v_\theta \\ v_\phi \end{bmatrix} = \begin{bmatrix} \sin\alpha\cos\beta & \cos\alpha\cos\beta & -\sin\beta \\ \sin\alpha\sin\beta & \cos\alpha\sin\beta & \cos\beta \\ \cos\alpha & -\sin\alpha & 0 \end{bmatrix}^{-1} \begin{bmatrix} v_x \\ v_y \\ v_z \end{bmatrix}, \tag{6}$$

where (v_r, v_θ, v_ϕ) are components of the filament vector in the local spherical coordinate. By definition, $(-\hat{\boldsymbol{u}}_\theta, \hat{\boldsymbol{u}}_\phi)$ is the sky image plane local to the point A (orange rectangle plane in Fig. 3) and $\hat{\boldsymbol{u}}_r$ is the normal vector of this plane. The inclination of the filament vector is the angle between $\boldsymbol{v}_{\rm fil}$ and the image plane. The position angle is the angle between $-\hat{\boldsymbol{u}}_\theta$, i.e. the local north vector, and the $\boldsymbol{v}_{\rm fil}$ projected

on to the image plane.

$$i_{\rm fil,img} = \arcsin\left(\frac{v_r}{\sqrt{v_r^2+v_\theta^2+v_\phi^2}}\right),$$
$$\mathrm{PA}_{\rm fil,img} = \arctan\left(-\frac{v_\phi}{v_\theta}\right). \quad (7)$$

Note that this position angle and inclination (as indicated by the notation '$_{\rm img}$') are specific to the image plane of the point A. This is because the coordinate basis $\hat{\boldsymbol{u}}_\phi$ is defined as a tangent vector of the equal declination line of the celestial sphere (green circle parallel to the x–y plane in Fig. 3) and therefore its vector magnitude $|\hat{\boldsymbol{u}}_\phi|$ is dependent on the declination of the point A. In contrast, $|\hat{\boldsymbol{u}}_r|$ and $|\hat{\boldsymbol{u}}_\theta|$ do not vary with changing locations on the sphere. In light of this, we use the generalized inclination and position angle in our analysis.

$$i_{\rm fil} = \arcsin\left(\frac{v_r}{\sqrt{v_r^2+v_\theta^2+\left(\frac{v_\phi}{\cos(\mathrm{Dec.})}\right)^2}}\right),$$
$$\mathrm{PA}_{\rm fil} = \arctan\left(-\frac{v_\phi}{v_\theta\cos(\mathrm{Dec.})}\right). \quad (8)$$

2.4 Sample selection

To study the alignment of optical galaxies, radio jets, and cosmic filaments, we select radio sources from the LoTSS optical cross-matched catalogue located within the cosmic volume covered by the SDSS filament catalogue. This means that, while the full LoTSS data come from two fields (RA-1 and RA-13), we limit our samples to sources in the RA-13 field (the peach-coloured shade in the top panel of Fig. 1).

Accurate redshift measurements of LoTSS sources are crucial in determining the location of radio sources with respect to cosmic filaments in 3D space. For sources in the LoTSS catalogue, both photometric and spectroscopic redshifts are provided, depending on availability. The 'z_best' and 'z_source' columns provide the best available redshift estimate and the origin of the best estimate, respectively. For the purpose of this study, we select sources with spectroscopic redshift measurement, from the SDSS DR16 (Ahumada et al. 2020), the DESI spectroscopic survey (DESI Collaboration 2024), or the Hobby-Eberly Telescope Dark Energy Experiment (HETDEX) data release (Mentuch Cooper et al. 2023).We limit the redshift of the LoTSS sources to $z < 0.6$ where the number density of the SDSS DR12 LOWZ + CMASS sample within the survey volume remains flat (see fig. 4 of Malavasi et al. 2020). Beyond $z > 0.6$, the filament identification is incomplete due to the limited sampling of the LOWZ + CMASS galaxy density field. Exclusively using sources with a spectroscopic redshift below 0.6 is crucial for our analysis as the accurate characterization of the 3D locations of radio sources and cosmic filaments is key to quantifying the cosmic environment in which the sources reside. As mentioned earlier, 60 per cent of the sources in the LoTSS DR2 radio-optical cross-matching catalogue have redshift measurements and are in the redshift range of $z < 0.6$. About 30 per cent of these redshift estimates are spectroscopic and the rest are photometric. For reference, the average error in the redshift measurement is 0.05 for the photometric redshift and 4×10^{-5} for the spectroscopic redshift. The selection of spectroscopic sample does not bias the results that will follow, since the availability of a spectroscopic redshift does not depend on key parameters probed in this study, namely the distance between a radio source and the closest cosmic filament defined by SDSS, the orientation of radio jets, and the orientation of the optical host galaxy.

Two samples are configured for different scientific purposes. The first is the general massive radio galaxy (GMRG) sample (blue markers in the top panel of Fig. 1, though most overlap with the green markers that correspond to the second sample explained in the paragraph below). The GMRG sample consists of radio sources matched with an extended optical galaxy (i.e. a galaxy with a measurable optical position angle) with a stellar mass $>10^{11}$ $\mathrm{M}_\odot$. In Section 3.1, we use this sample to investigate the alignment of the galaxy's optical major axis and the cosmic filament orientation. There are 73 077 sources that satisfy the selection criteria for the GMRG sample.

Secondly, we define the EJ sample as a subset of the GMRG sample that shows bright, extended (i.e. sources with a measurable radio position angle) radio jets (green markers in Fig. 1). We use the EJ sample to investigate the alignment between radio jets and their host galaxies in Section 3.2. We impose selection criteria for the EJ sample based on the radio properties as follows. In total, there are 6270 sources matching the selection criteria.

(i) High signal-to-noise ratio: 'Peak_flux'/'Isl_rms' > 10, where 'Peak_flux' is the 144 MHz peak flux density and 'Isl_rms' is the local root-mean-square noise.

(ii) High radio luminosity: 'L_144' $> 10^{24}$ W Hz^{-1}, where 'L_144' is the radio luminosity estimated from the total flux density of the source assuming a spectral index of 0.7.[5]

(iii) Large angular size: 'LAS' > 20 arcsec and 'Resolved' == True, where 'LAS' is the angular size estimated using a method specified in the 'LAS_from' column. The 'Resolved' column is based on the resolution criterion of Shimwell et al. (2022) and ensures a reliable measurement of 'LAS'.

(iv) Reliable radio position angle measurement: For 'S_Code' = 'M' sources, 'E_PA' $< 5^\circ$, where 'E_PA' is the error in $\mathrm{PA}_{\rm radio}$; for 'S_Code' = 'Z' sources, 'Blend_prob' < 0.2 and 'Other_prob' < 0.2, where 'Blend_prob' and 'Other_prob' are the probabilities for the source being blended or problematic. Furthermore, we use supplementary tags provided by RGZ(L) to identify radio sources with complex morphology and remove them from the final sample since the position angles of such sources often do not correctly trace the direction of jets at launch; any sources with 'nat', 'blend', 'bent', 'wat', 'x-shaped', 's-shaped', and 'v-shaped' tags have been removed. However, it should be noted that this does not remove all complex-morphology radio sources in our sample, as these tags are not consistently applied to all sources in LoTSS DR2 (Hardcastle et al. 2023).

The top panel of Fig. 4 shows the stellar mass distribution of the GMRG and EJ samples. All our sample galaxies are $11 < \log M_*/\mathrm{M}_\odot < 12.33$. The stellar mass of the EJ sample is on average higher than the GMRG sample. This trend is well known, as powerful radio galaxies have long been associated with being hosted by the most massive galaxies, which contain the most massive black holes (Jarvis et al. 2001; McLure & Jarvis 2004; Herbert et al. 2011; Whittam et al. 2022).

We also show histograms of the angular separation ($\theta_{\rm fil}$, middle panel) and the physical distance ($D_{\rm fil}$, bottom panel) between radio sources and their closest cosmic filament sampling point identified following the method described in Section 2.3. The long tails of the distributions towards the large $\theta_{\rm fil}$ and $D_{\rm fil}$ values include not only

[5]The spectral index, $\alpha_{\rm spec}$, is related to flux density S_ν by $S_\nu \propto \nu^{-\alpha_{\rm spec}}$.

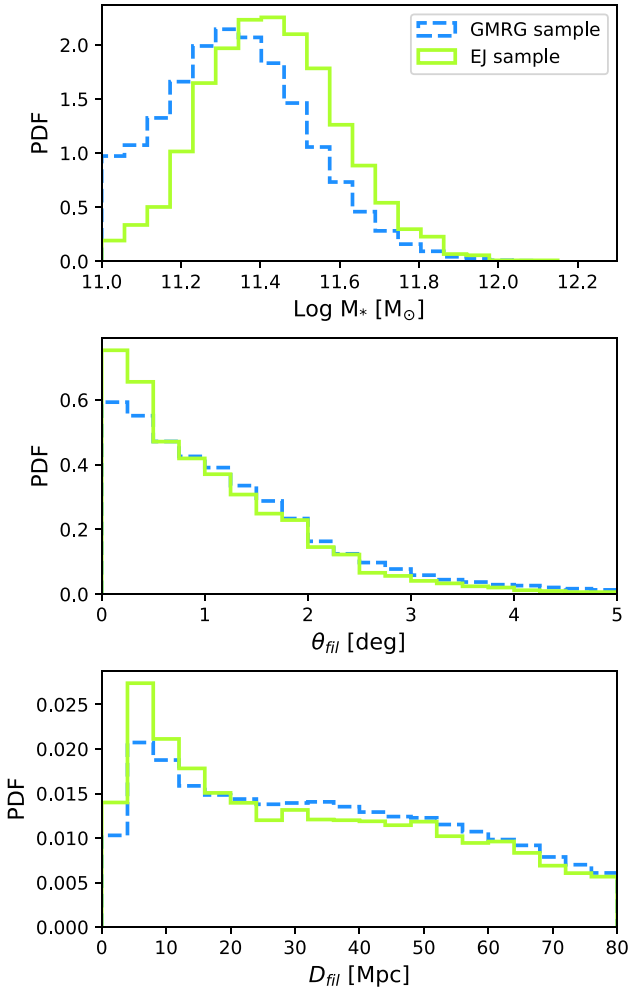

Figure 4. Histograms showing the stellar mass distribution (top panel) and the angular/physical distance from the closest filament distribution (middle/bottom panel) of the GMRG (dashed line) and EJ (solid line) samples. Note that the EJ sample is a subset of the GMRG sample and $\theta_{\rm fil}$ and $D_{\rm fil}$ are the angular and physical separations, respectively, to the closest filament matched to a galaxy based on the 3D locations.

extremely isolated galaxies in the voids but also galaxies close to less prominent filaments that are not picked up by the DisPerSE filament finder. In this study, we limit the samples to galaxies within $D_{\rm fil} < 80$ Mpc, which is significantly larger than the typically expected impact radius of cosmic filaments (Bond, Strauss & Cen 2010; Cautun et al. 2014; Bonjean et al. 2020; Galárraga-Espinosa et al. 2020; Wang et al. 2024). By doing so, we omit galaxies that are close to unidentified filaments that potentially bear the imprint of filaments on their physical properties. Yet, there are already a sufficient number of galaxies close to the prominent filaments to obtain the statistical significance of the results presented in this paper.

3 RESULTS

3.1 Alignment between optical galaxy and cosmic filament

In this section, we examine the alignment of optical galaxies with their nearest cosmic filaments using the GMRG sample.

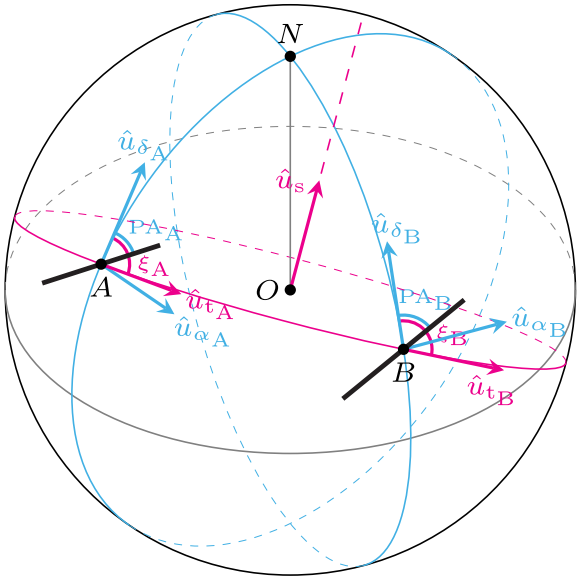

Figure 5. An illustration of parallel transport method. In this illustration, there are two blue-coloured great circles connecting the North celestial pole (N) and the points A and B, respectively. Angles $\mathrm{PA_A}$ and $\mathrm{PA_B}$ are the position angles of the two black bars at each point, measured from the local north vectors ($\hat{\boldsymbol{u}}_{\delta_{\rm A}}$ and $\hat{\boldsymbol{u}}_{\delta_{\rm B}}$). The pink circle is the great circle connecting A and B. Angles $\xi_{\rm A}$ and $\xi_{\rm B}$ are the angle between the local north vector and the tangent vector of the pink great circle ($\hat{\boldsymbol{u}}_{\rm t_A}$ and $\hat{\boldsymbol{u}}_{\rm t_B}$) at points A and B, respectively. For further explanation of the parallel transport method, see the text in Section 3.1.1.

3.1.1 Parallel transport method

As shown in Fig. 4, a galaxy and the closest filament sampling point can be separated by significant angular distances in some cases. In this case, the position angles of the galaxy and the filament orientation should be compared with extra care. Fig. 5 illustrates how we correctly compare two position angle measurements ($\mathrm{PA_A}$ and $\mathrm{PA_B}$) at two points on the celestial sphere, A and B, using the parallel transport method (Jain, Narain & Sarala 2004; Contigiani et al. 2017; Osinga et al. 2020; Mandarakas et al. 2021). The blue great circles intersecting at point N (north) are the local meridians at A and B. The bold black bar at A and B represents the orientation of the object of interest. The position angle of a source is, by definition, measured from the axis pointing north along the local meridian. Therefore, the vector of the black bar at location A can be expressed as

$$\boldsymbol{v}_{\rm A} = \sin(\mathrm{PA_A})\hat{\boldsymbol{u}}_{\alpha_{\rm A}} + \cos(\mathrm{PA_A})\hat{\boldsymbol{u}}_{\delta_{\rm A}}, \tag{9}$$

where $\hat{\boldsymbol{u}}_{\alpha_{\rm A}}$ and $\hat{\boldsymbol{u}}_{\delta_{\rm A}}$ are the unit vectors local to the location A pointing at north and east, respectively. Similarly, the vector at point B is written as

$$\boldsymbol{v}_{\rm B} = \sin(\mathrm{PA_B})\hat{\boldsymbol{u}}_{\alpha_{\rm B}} + \cos(\mathrm{PA_B})\hat{\boldsymbol{u}}_{\delta_{\rm B}}. \tag{10}$$

Since the points A and B have non-negligible separation in the RA axis, the north vectors $\hat{\boldsymbol{u}}_{\delta_{\rm A}}$ and $\hat{\boldsymbol{u}}_{\delta_{\rm B}}$ point at different directions in the absolute reference frame. The parallel transport method exploits the fact that the angle between the orientation vectors, $\boldsymbol{v}_{\rm A}$ and $\boldsymbol{v}_{\rm B}$, and vectors tangential to the great circle connecting the two locations (the pink-coloured circle intersecting with A and B) is invariant for parallel transport to any location along this great circle. The normal

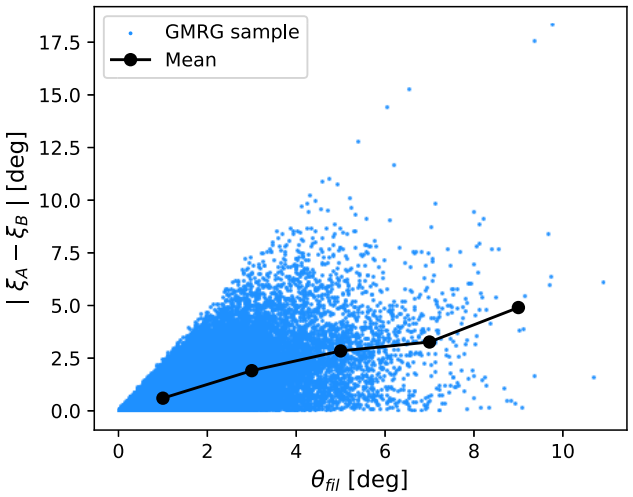

Figure 6. The degree of parallel transport applied to the GMRG sample as a function of the angular separation between the optical galaxy and the filament ($\theta_{\rm fil}$). Each data point corresponds to one GMRG sample galaxy. The line shows the mean value of $|\xi_{\rm A} - \xi_{\rm B}|$ at a given $\theta_{\rm fil}$ window size of 2°.

vector of this great circle is

$$\hat{\boldsymbol{u}}_{\rm s} = \frac{\hat{\boldsymbol{u}}_{\rm A} \times \hat{\boldsymbol{u}}_{\rm B}}{|\hat{\boldsymbol{u}}_{\rm A} \times \hat{\boldsymbol{u}}_{\rm B}|}, \tag{11}$$

where $\hat{\boldsymbol{u}}_{\rm A}$ and $\hat{\boldsymbol{u}}_{\rm B}$ are unit radial vectors pointing at points A and B, respectively. The unit vectors tangential to the great circle at points A and B are

$$\hat{\boldsymbol{u}}_{\rm t_A} = \hat{\boldsymbol{u}}_{\rm s} \times \hat{\boldsymbol{u}}_{\rm A} \tag{12}$$

and

$$\hat{\boldsymbol{u}}_{\rm t_B} = \hat{\boldsymbol{u}}_{\rm s} \times \hat{\boldsymbol{u}}_{\rm B}, \tag{13}$$

respectively. The angle between the local north vectors and the tangent vectors can be expressed as

$$\xi_{\rm A} = \arccos\left(\hat{\boldsymbol{u}}_{\delta_{\rm A}} \cdot \hat{\boldsymbol{u}}_{\rm t_A}\right) \tag{14}$$

and

$$\xi_{\rm B} = \arccos\left(\hat{\boldsymbol{u}}_{\delta_{\rm A}} \cdot \hat{\boldsymbol{u}}_{\rm t_B}\right). \tag{15}$$

The angles $\xi_{\rm A}$ and $\xi_{\rm B}$ quantify the change of the local RA and Dec. basis with respect to the great circle. Transporting the orientation vector $\boldsymbol{v}_{\rm A}$ to the location B makes a vector $\boldsymbol{v}'_{\rm A}$ with the following position angle with respect to the local meridian at B:

$$\mathrm{PA}'_{\rm A} = \mathrm{PA}_{\rm A} - \xi_{\rm A} + \xi_{\rm B}. \tag{16}$$

Fig. 6 shows the absolute degree of parallel transport, i.e. $|\xi_{\rm A} - \xi_{\rm B}|$, we apply when comparing the optical position angles of the GMRG sample (blue markers) to the position angle of the closest filament. The black line is the mean profile of the distribution. On average, parallel transport alters the position angles of the GMRG galaxies by $\lesssim 3°$.

Finally, the dot product between the two orientation vectors leads to

$$\boldsymbol{v}'_{\rm A} \cdot \boldsymbol{v}_{\rm B} = \cos\left(\mathrm{PA}_{\rm A} - \mathrm{PA}_{\rm B} - \xi_{\rm A} + \xi_{\rm B}\right); \tag{17}$$

i.e. the true angle between the two orientation vectors at points A and B is $\mathrm{PA}_{\rm A} - \mathrm{PA}_{\rm B} - \xi_{\rm A} + \xi_{\rm B}$. Note that, by definition, $\mathrm{PA}_{\rm A}$ and $\mathrm{PA}_{\rm B}$ range $[0, 180]°$. When we refer to the angle between two orientations in the following paragraphs, we wrap the angles between $[0, 90]°$ as we do not define a direction for the filament or jet orientation.

3.1.2 *Results: galaxy–filament alignment in cosmic filaments*

The top panel of Fig. 7 shows histograms of the angle between the galaxy major axis and the orientation of the closest filament. Angles close to zero indicate that galaxies are elongated along the direction of the filament. Note that a uniform distribution is expected for the angle between two randomly oriented 2D vectors on the sky plane. The blue line represents all GMRG sample galaxies within $D_{\rm fil} < 80$ Mpc. We find that this distribution is consistent with being uniform between 0 and 90°. The other lines are the histograms of the filament–galaxy angle in different ranges of $D_{\rm fil}$, shifted along the y-axis for better visibility. The sample is binned to contain roughly the same number of galaxies in each $D_{\rm fil}$ range. Although the distribution is nearly uniform in most binned samples, there is a subtle excess towards 0° among galaxies close to the filaments ($D_{\rm fil} \leqslant 6.33$ Mpc).

In order to quantify the excess, we calculate the skewness of each distribution defined as

$$G_1 = \frac{\sqrt{N(N-1)}}{N-2} \frac{m_3}{m_2^{3/2}}, \tag{18}$$

i.e. the adjusted Fisher–Pearson coefficient, where

$$m_i = \frac{1}{N} \Sigma_{i=1}^{N} (x_i - \bar{x})^i, \tag{19}$$

N is the total number of galaxies in each sample, and $\bar{x}$ is the sample mean. The bottom left panel of Fig. 7 shows the skewness of the distribution in each $D_{\rm fil}$ bin. The error bars are the 95 per cent confidence level obtained by bootstrap resampling 10 000 times. The dashed horizontal line in pink colour indicates the zero skewness as a reference. We confirm that the filament–galaxy angle distribution is positively skewed within $D_{\rm fil} \leqslant 10.94$ Mpc. The skewness is the highest in the bin closest to the filament ($D_{\rm fil} \leqslant 6.33$ Mpc). At large distances beyond $D_{\rm fil} > 10.94$ Mpc, the skewness fluctuates around zero.

We perform the Kolmogorov–Smirnov (KS) test to examine the statistical significance of our findings. First, we use the one-sample KS test to compare the filament–galaxy angle distribution in each distance bin with the uniform distribution. In the bottom right panel of Fig. 7, we show the p-value of the KS test in each bin with a solid horizontal line spanning the corresponding $D_{\rm fil}$ range. The dashed horizontal line in pink colour is a p-value of 0.05 for reference. The p-value is 0.000 43 in $D_{\rm fil} \leqslant 6.33$ Mpc and 0.0201 in 6.33 Mpc $< D_{\rm fil} \leqslant 10.94$ Mpc. In both cases, we reject the null hypothesis that the filament–galaxy angle distribution is uniform with a confidence level of $\gtrsim$99 per cent. In larger $D_{\rm fil}$ ranges, all p-values are greater than 0.05. We cannot reject the hypothesis that these distributions are uniform.

We also perform the two-sample KS test comparing the distributions within the first bin ($D_{\rm fil} \leqslant 6.33$ Mpc) and the rest of the sample (6.33 Mpc $< D_{\rm fil} <$ 80 Mpc). The p-value of this test is 0.0012 (the red star symbol in the first $D_{\rm fil}$ bin in Fig. 7). We therefore reject the null hypothesis that the distribution of filament–galaxy angle in the $D_{\rm fil} \leqslant 6.33$ Mpc bin is drawn from the same underlying distribution as the rest of the sample with a confidence level of >99 per cent.

To test whether there is a stellar mass dependency in the filament–galaxy alignment we find close to filaments, we further divide the GMRG sample into low-mass ($11 < \log M_*/\mathrm{M}_\odot \leqslant 11.4$) and high-mass ($11.4 < \log M_*/\mathrm{M}_\odot$) populations. The top panel of Fig. 8 shows the skewness of the filament–galaxy angle distribution of the two subsamples (low-mass: black line, high-mass: yellow line) in different $D_{\rm fil}$ bins. The blue line shows the result from the entire GMRG sample regardless of the stellar mass (i.e. same as the line shown in the bottom left panel of Fig. 7), for reference. Only

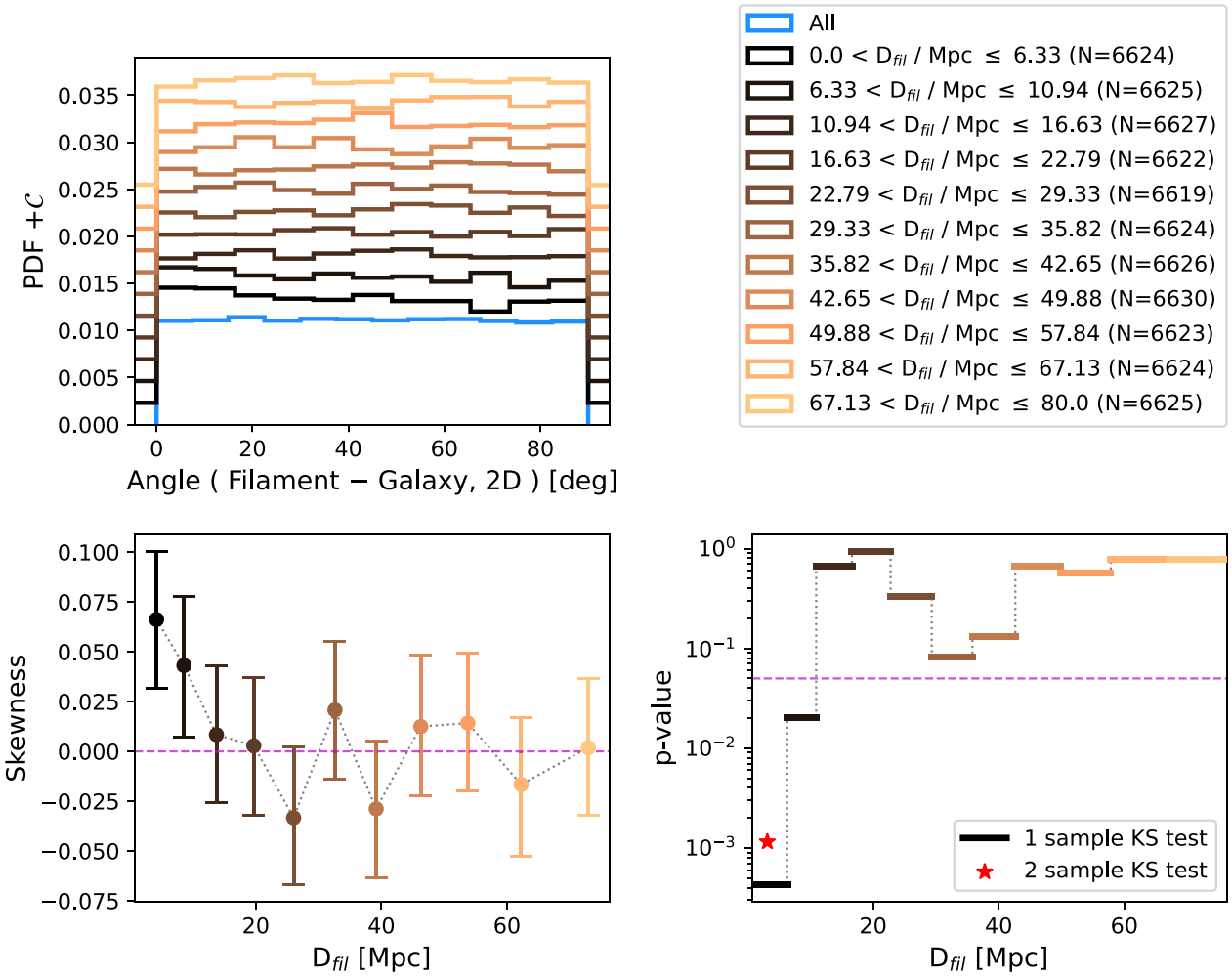

Figure 7. The distribution of the angle between the galaxy optical major axis and the closest filament orientation as a function of the distance to the filament. The GMRG sample is used for this analysis. Top panel: The histogram between [0, 90]°. The blue line represents the distribution of all GMRG sample galaxies. All other coloured lines correspond to different $D_{\rm fil}$ bins. All histograms are vertically shifted, as denoted by $\mathcal{C}$ on the y-axis label, for better visibility. The $\mathcal{C}$ value is different for each histogram and can be determined by the y-axis value in the negative x-axis range. Bottom left panel: The skewness of the galaxy–filament angle distribution in different $D_{\rm fil}$ bins. The positive (negative) skewness indicates that the distribution is skewed towards 0° (90°). The horizontal dashed line shows where the skewness is zero. Bottom right panel: The thick horizontal lines show the p-values of one-sample KS tests comparing the uniform distribution and the filament–galaxy angle distribution in each bin. The red star symbol in the first bin shows the p-value of a two-sample KS test comparing the filament–galaxy angle distributions in $D_{\rm fil} \leqslant 6.33$ Mpc and $D_{\rm fil} > 6.33$ Mpc ranges. The horizontal dashed line shows where the p-value is 0.05.

the inner $D_{\rm fil} < 25$ Mpc range is shown for visualization. In the innermost bin ($D_{\rm fil} \leqslant 6.33$ Mpc), we find that higher mass galaxies have higher skewness in the filament–galaxy angle distribution than the lower mass galaxies. We perform a two-sample KS test and find that the filament–galaxy angle distributions of the two populations are statistically different with a p-value of 0.0002. This result demonstrates that the alignment between galaxies and their closest filament is stronger for more massive galaxies near filaments.

Next, we investigate whether the systematic galaxy–filament alignment among galaxies close to filaments depends on the optical ellipticity of the galaxy, $|\epsilon_{\rm opt}|$ (see equation 1 for the definition of $\epsilon_{\rm opt}$). The middle panel of Fig. 8 shows the skewness of the filament–galaxy angle distribution at different $D_{\rm fil}$ bins with the GMRG sample divided into two subsamples depending on the optical ellipticity: $|\epsilon_{\rm opt}| \leqslant 0.1$ (black line) and $|\epsilon_{\rm opt}| > 0.1$ (yellow line). We find that the increase in the skewness at the innermost bin ($D_{\rm fil} \leqslant 6.33$ Mpc) compared to the other bins is higher for the sample with higher optical ellipticities. The p-value of the one-sample KS test between the uniform distribution and the filament–galaxy angle distribution at $D_{\rm fil} \leqslant 6.33$ Mpc and $|\epsilon_{\rm opt}| > 0.1$ is 3×10^{-5}. In contrast, galaxies with $|\epsilon_{\rm opt}| \leqslant 0.1$ do not reveal any sign of systematic alignment with their closest filament in the skewness at all distances. The p-value of the one-sample KS test, in this case between the uniform distribution and the filament–galaxy angle distribution at $D_{\rm fil} \leqslant 6.33$ Mpc and $|\epsilon_{\rm opt}| \leqslant 0.1$, is 0.39.

Finally, we test whether the observed galaxy–filament alignment depends on the inclination of cosmic filaments ($i_{\rm fil}$) with respect to the sky plane. A higher $i_{\rm fil}$ means that the filaments are well aligned with the radial sightline, and a lower $i_{\rm fil}$ means that the filaments are parallel to the sky plane. The bottom panel of Fig. 8 shows the skewness of the filament–galaxy angle distribution at different $D_{\rm fil}$ bins, with samples divided into $i_{\rm fil} \leqslant 45°$ (black line) and $i_{\rm fil} > 45°$ (yellow line). In the innermost bin ($D_{\rm fil} \leqslant 6.33$ Mpc), we find that the sample with $i_{\rm fil} \leqslant 45°$ shows higher skewness than its low-inclination counterpart. The one-sample KS test rejects the null hypothesis that the filament–galaxy angle distribution is uniform (p-value of 2.4 ×

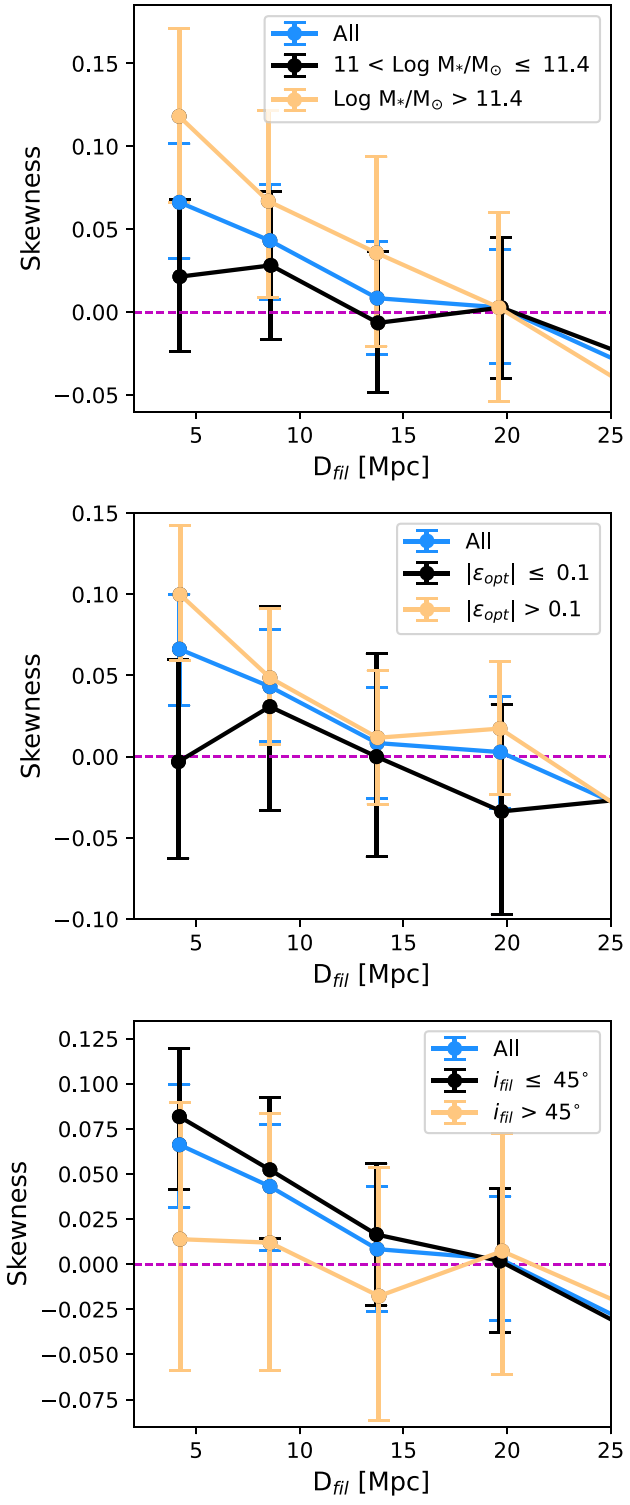

Figure 8. The skewness of the galaxy–filament angle distribution in different $D_{\rm fil}$ bins. In all panels, the blue line shows the skewness calculated using all galaxies in the GMRG sample, i.e. the result shown in the bottom left panel of Fig. 7. Top panel: The effect of varying stellar mass (black: $11 < \log M_*/{\rm M}_\odot \leqslant 11.4$, yellow: $\log M_*/{\rm M}_\odot > 11.4\,{\rm M}_\odot$). Middle panel: The effect of varying optical ellipticity (black: $|\epsilon_{\rm opt}| \leqslant 0.1$, yellow: $|\epsilon_{\rm opt}| > 0.1$). Bottom panel: The effect of varying filament inclination (black: $i_{\rm fil} \leqslant 45^\circ$, yellow: $i_{\rm fil} > 45^\circ$).

10^{-4}) in this sample. For the sample with $i_{\rm fil} > 45^\circ$, the skewness is close to zero in all $D_{\rm fil}$ ranges. The p-value of the one-sample KS test between the uniform distribution and the filament–galaxy angle distribution at $D_{\rm fil} \leqslant 6.33$ Mpc and $i_{\rm fil} > 45^\circ$ is 0.69.

In brief summary, we find strong evidence that the galaxies in the cosmic filament environment ($D_{\rm fil} \lesssim 11$ Mpc) have their major axis aligned with the orientation of the filaments. The alignment is stronger among galaxies with higher mass and higher optical ellipticity and filaments with smaller inclinations (i.e. more parallel to the sky plane). In Section 4.1.1, we will discuss physical mechanisms that produce mass-dependent filament–galaxy alignment and explain the $\epsilon_{\rm opt}$ and $i_{\rm fil}$ dependences based on (i) the projection effect; (ii) the intrinsic shape of galaxies; and (iii) observational uncertainty in the 3D orientation of filaments as well as the optical position angle.

3.2 Alignment between optical galaxy and radio jet

In this section, we investigate the angle between the radio jets in the EJ sample and the major axis of their optical host galaxies. Our motivation to do so is to understand whether the optical galaxy–cosmic filament alignment within the filaments we find in the previous section is due to a direct connection between the evolution of a galaxy's stellar component and cosmic filaments or whether it is a secondary correlation that arises from interactions between radio jets and the intergalactic medium (IGM), along with the relationship between jet and galaxy orientations. Unlike the previous analysis comparing the orientations of filaments and galaxies, we do not implement the parallel transport method in this case, as the angular separations between the cross-matched radio and optical pairs are co-spatial.

First, we examine the effect of optical ellipticity on the jet–galaxy alignment. The top left panel of Fig. 9 shows the histograms of the jet–galaxy angle in different optical ellipticity bins. The green line represents the entire EJ sample. The distribution peaks at 90°, indicating that the radio jets tend to align perpendicularly to the galactic major axis in general. Histograms in other colours that represent different optical ellipticity bins are shifted along the y-axis for better visibility. For galaxies in the lowest ellipticity range, i.e. $|\epsilon_{\rm opt}| < 0.07$, the angle between the radio jet and the optical major axis is nearly randomly distributed between 0 and 90° (see the histogram in the black line, which is close to the uniform distribution). With increasing ellipticity, the histograms show a stronger peak at 90°. The skewness of the jet–galaxy angle distribution is presented in the bottom left panel of Fig. 9. This result further confirms the trend: with increasing $|\epsilon_{\rm opt}|$, the distribution is more negatively skewed, i.e. more strongly skewed towards 90°. This result aligns with previous findings of Zheng et al. (2024), where the authors find stronger alignment between radio jets and optical minor axis among galaxies with smaller optical minor-to-major axes ratio (e.g. see fig. 10 of their paper). In their paper, the authors have shown that this trend is not entirely the projection effect but due to the intrinsic alignment of jets to the minor axis of an oblate galaxy.

Similarly, the results of the one-sample KS test shown in the bottom right panel of Fig. 9 confirm that the p-values of the test decrease significantly with increasing $|\epsilon_{\rm opt}|$. This means that we can reject the null hypothesis that the jet–galaxy angles are drawn from the uniform distribution with an increasingly higher confidence level as the optical ellipticity increases. None the less, p-values are always lower than 0.05 in all $|\epsilon_{\rm opt}|$ ranges; the jet–galaxy angle distribution is always non-uniform at a confidence level of 95 per cent.

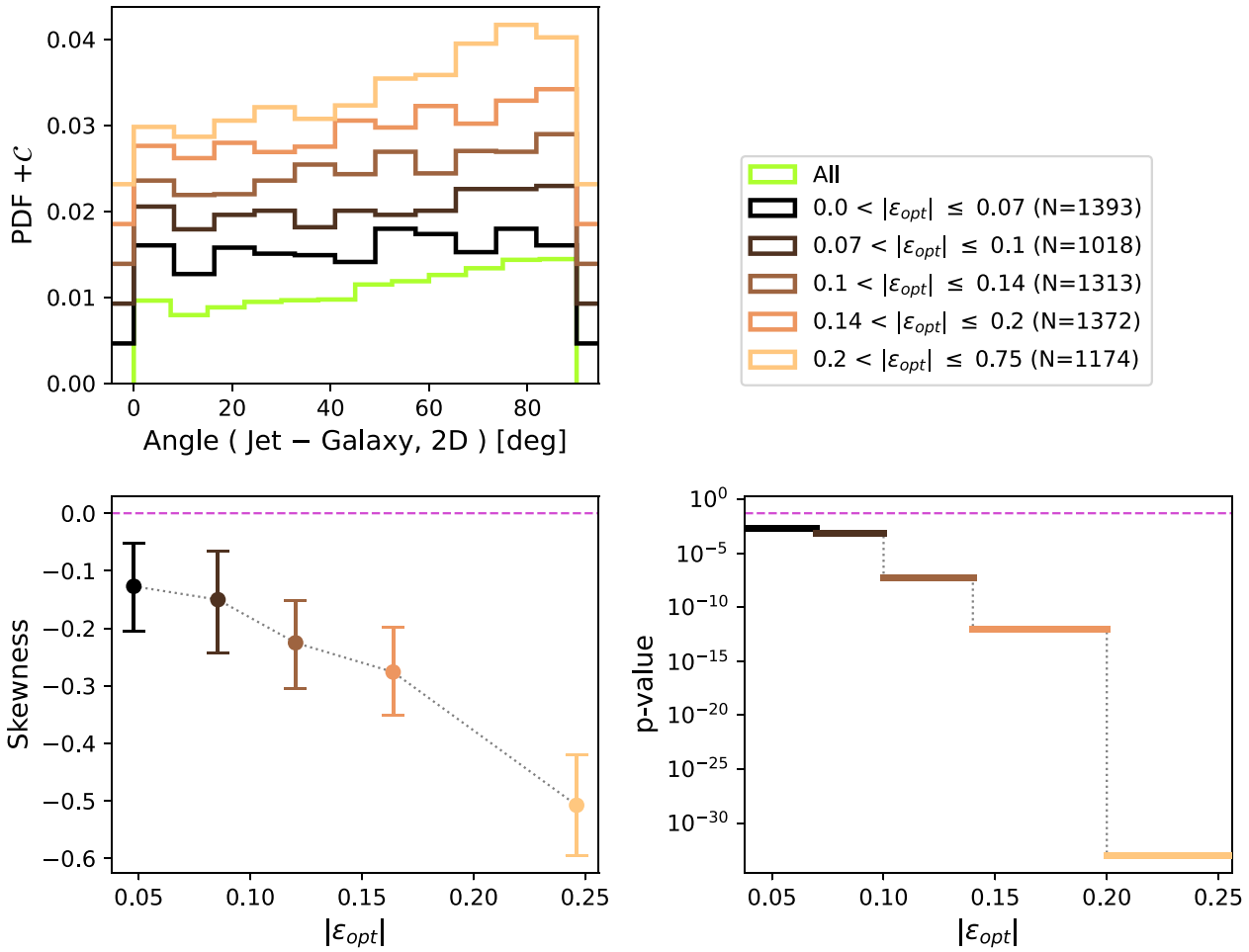

Figure 9. The distribution of the angle between the galaxy optical major axis and the radio jet orientation as a function of the optical ellipticity. The EJ sample is used for this analysis. The panels are in the same format as Fig. 7.

Based on the above results, we select a subset of EJ sample galaxies with $|\epsilon_{\rm opt}| > 0.1$ as a subsample with substantial bias towards having a jet perpendicular to the galaxy major axis. We confirm that the exact choice of the lower limit of $|\epsilon_{\rm opt}|$ does not significantly affect the results presented in this paper. For the remainder of this section, we investigate whether cosmic filaments have an effect on this bias. It is worth mentioning that $|\epsilon_{\rm opt}|$ of the EJ sample galaxies does not depend on the distance to the nearest filament. Therefore, the variation in the jet–galaxy alignment with respect to the distance to the filament, which we will present shortly, is not due to the trend in ellipticity.

In Fig. 10, we show the jet–galaxy angle distribution in various $D_{\rm fil}$ bins in the same format as Figs 7 and 9. As can be noticed from histograms in the top left panel and the skewness distribution in the bottom left panel, the distribution of jet–galaxy angle is less strongly peaked at 90° in the bin closest to filaments ($D_{\rm fil} \leqslant 8.06$ Mpc) compared to the other larger distance ranges. The skewness of the distribution is the lowest in this $D_{\rm fil}$ range. The skewness remains nearly constant in all other $D_{\rm fil}$ ranges beyond 8.06 Mpc.

An alternative way to quantify the jet–galaxy angle distribution is to calculate the fraction of galaxies with 'misaligned' jets. Supposing jets are intrinsically aligned with the optical minor axis, we consider them to be misaligned if the position angle is more than 30° away from the optical minor axis (<60° in the histogram since the angle in Fig. 10 is measured from the optical major axis). We find that $\approx 59.8^{+3.7}_{-3.9}$ per cent of the EJ galaxies have misaligned jets at $D_{\rm fil} \leqslant 8.06$ Mpc. The fraction decreases to $\approx 55.9^{+1.7}_{-1.7}$ per cent at larger distance. Potentially, the fraction of misaligned jets will be larger among galaxies even closer to filament spines than 8.06 Mpc. However, we could not confirm the statistical significance due to the limited sample size.

The bottom right panel of Fig. 10 shows the outcomes of the KS tests. The p-values of the one-sample KS tests (solid horizontal lines) are always lower than 0.05 (dashed horizontal line). This means that, regardless of the distance to the closest filament, we reject the null hypothesis that the jet–galaxy angles are drawn from the uniform distribution with a 95 per cent confidence level. This is expected since, as mentioned above, we have purposely selected a subpopulation of the EJ sample that is supposed to show a clear preference for the jets being perpendicular to the galaxy major axis. The p-value of the two-sample KS test between the jet–galaxy angle distribution of galaxies in $D_{\rm fil} \leqslant 8.06$ Mpc and > 8.06 Mpc is 0.041 (red star symbol). We reject the null hypothesis that the jet–galaxy angles in two $D_{\rm fil}$ ranges are drawn from the same distribution with a 95 per cent confidence level.

Based on the results presented in this section, we conclude that galaxies in the cosmic filament environment ($D_{\rm fil} \leqslant 8.06$ Mpc) have radio jets that are more randomly oriented with respect to the galaxy optical major axis than galaxies at larger distances to filaments. Still, the jet direction is not entirely random.

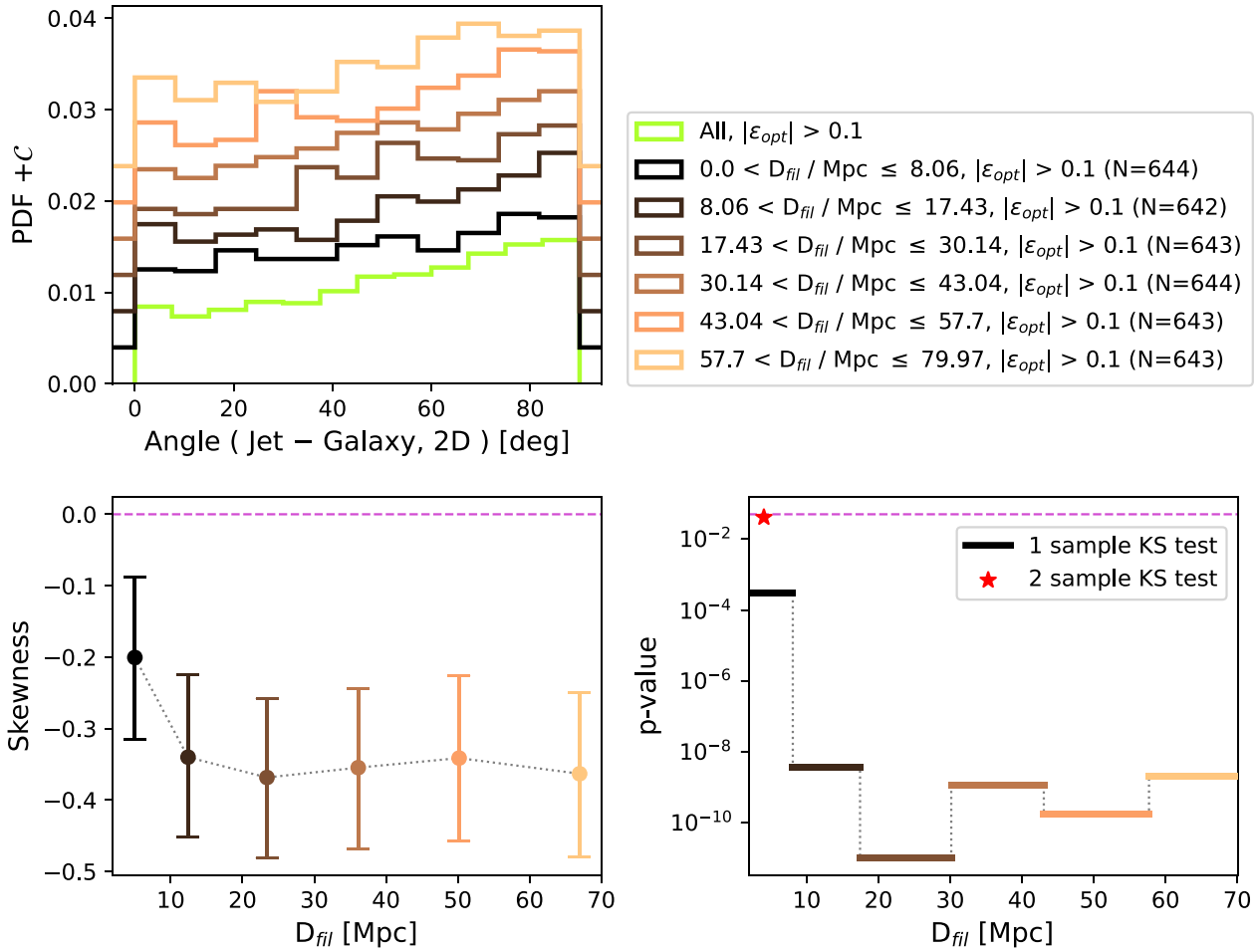

Figure 10. The distribution of the angle between the galaxy optical major axis and the radio jet orientation as a function of the distance to the filament. The EJ sample is used for this analysis. The panels are in the same format as Fig. 7.

4 DISCUSSION

4.1 Physical picture

Probing the alignment between radio jets, optical galaxies, and the large-scale structure provides interesting insight into galaxy evolution. The direction of radio jets is related to the accretion mode of the central black hole as will be explained in detail later in this section. The observed shape of optical galaxies is closely related to their stellar kinematics shaped by the underlying gravitational potential of their halo, as well as their past star formation and merger events. Cosmic filaments shape the large-scale matter flow pattern surrounding galaxies. In this section, we summarize previous theoretical studies that explain the alignment/misalignment of (i) galaxies with respect to cosmic filaments and (ii) AGN jets with respect to galaxies. We then discuss how the results presented in Section 3 fit into the physical picture.

4.1.1 Mechanisms for filament–optical galaxy alignment

In numerical simulations, dark matter haloes are found to be more intrinsically elongated and prolate with increasing mass (Bett et al. 2007; Tenneti et al. 2014). This suggests that the build-up of these massive haloes is affected by directional, filamentary accretion of mass (Allgood et al. 2006; Vera-Ciro et al. 2011). Although it has been reported that massive haloes experience a transition of accretion pattern throughout their evolution from directional to isotropic accretion (Allgood et al. 2006), the directional accretion is still significant in cosmic filament environments where haloes travel along the filaments towards denser nodes and collide with each other. In this case, the direction of mergers, accretion, and fly-bys that haloes experience throughout their evolution is predominantly aligned with the orientation of the cosmic filament. As a result, the major axis of haloes tends to align with the cosmic filaments in which they are embedded, and the significance of the alignment increases with halo mass (Lee et al. 2008; Zhang et al. 2009; Libeskind et al. 2014; Kang & Wang 2015; Morinaga & Ishiyama 2020).

The alignment between galaxies and cosmic filaments should be interpreted in a similar context. In the stellar mass range probed in this study, $\log M_*/M_\odot > 11$, galaxies and their host halo grow by numerous mergers, and there is a high fraction of dispersion-dominated slow-rotating galaxies (Emsellem et al. 2011; van de Sande et al. 2017; Veale et al. 2017). These systems are flattened by the anisotropic velocity dispersion of the stars rather than by their rotational motion (Binney 1978; Binney & Tremaine 2008). For that reason, the optical position angle of the galaxies we use in this study is closely related to the shape of the gravitational potential and the orbital angular momentum of previously accreted subhaloes/galaxies. In the following paragraphs, we discuss how our results support the scenario that, for galaxies that reside within the

cosmic filament environment, mergers have occurred predominantly along the direction of the filaments.

In Section 3.1, we find that the optical major axis of galaxies within 11 Mpc of cosmic filaments is systematically oriented parallel to the closest cosmic filament. If this galaxy–filament alignment is caused by physical processes, especially those that are related to mergers and accretions, one can expect the following tendency: (i) The alignment is strong within the cosmic filaments and non-existent outside the boundary of filaments; (ii) the significance of alignment depends on the stellar mass as filament galaxies with different stellar masses have different assembly histories; and (iii) the projection effect affects the significance of the alignment signal observed on the 2D sky plane. Indeed, we confirm that these trends are present in our sample. First, we find that the galaxy–filament alignment is the strongest among galaxies closer than $\lesssim$6 Mpc from the filaments (see Fig. 7). There is a weaker sign of alignment between 6 and 11 Mpc of the filaments. Beyond 11 Mpc, galaxies are randomly oriented with respect to the matched filament because there is no preferred direction of mergers set by nearby filaments. From this result, we can infer that the characteristic radius of cosmic filaments, where directional mergers and accretion take place, is $\lesssim$6–11 Mpc. This result is in broad agreement with previous investigations on the characteristic radius of filaments (e.g. Bond et al. 2010; Cautun et al. 2014; Bonjean et al. 2020; Galárraga-Espinosa et al. 2020), though the exact scale is subject to the definition of the boundary (Wang et al. 2024).

Secondly, the mass dependence of the galaxy–filament alignment is clearly visible in the top panel of Fig. 8. The stronger alignment of the galaxy major axis with the filament we find among more massive galaxies ($11.4 < \log M_*/\mathrm{M}_\odot$) within filaments ($\lesssim$6 Mpc) reflects the assembly history of these galaxies, which likely have grown by numerous mergers and accretion events along the filament. In contrast, we find no alignment signal among the lower mass galaxies ($11 < \log M_*/\mathrm{M}_\odot < 11.4$). While some studies suggest that the alignment of galaxy/halo major axis transitions with increasing mass from being perpendicular to filaments to being parallel (or the spin axis transitions from parallel to perpendicular; Aragón-Calvo et al. 2007; Codis et al. 2012; Libeskind et al. 2013; Trowland, Lewis & Bland-Hawthorn 2013), the stellar mass range probed in this work ($>10^{11}$ $\mathrm{M}_\odot$) is beyond the typically suggested transition mass (e.g. $M_* \gtrsim 3 \times 10^{10}\,\mathrm{M}_\odot$; Dubois et al. 2014). Therefore, we do not expect the filament–galaxy angle distribution to skew towards 0°, even among the lowest stellar mass galaxies in our sample.

Finally, we test the projection effect by comparing the significance of the observed galaxy–filament alignment depending on the inclination of the filaments and the galaxy ellipticity (see the middle and bottom panels of Fig. 8). The idea is that filaments with close-to-zero inclination, i.e. filaments oriented along the plane of the sky, will reveal an alignment as strong as the 3D alignment intrinsically arising from physical processes, whereas filaments with their inclination close to 90° will not reveal any sign of alignment since the intrinsic 3D axis of alignment is parallel to the line of sight. Similarly, edge-on galaxies will show a stronger alignment on the sky plane than face-on galaxies, as their intrinsic major axis is parallel to the plane of the sky. Although we do not have a direct tracer for the inclination of optical galaxies, we take advantage of the fact that at a given intrinsic ellipticity, higher projected ellipticity corresponds to higher galaxy inclination, i.e. the edge-on view. We find a stronger galaxy–filament alignment in the cosmic filament environment with increasing optical ellipticity and decreasing filament inclination. This further supports our conclusion that the galaxy–filament alignment is of physical origin.

Note that galaxies with higher optical ellipticity can also be the ones with higher intrinsic ellipticity. In this case, the stronger major axis alignment with filaments among galaxies with higher optical ellipticity can be interpreted such that more intrinsically elongated galaxies have a stronger alignment with cosmic filaments. The higher intrinsic ellipticity might indicate a more coherent direction of mergers throughout the assembly of galaxies. However, it is beyond the scope of this paper to separate how much of the optical ellipticity dependence of the galaxy–filament alignment comes from the projection effect and the change in intrinsic ellipticity.

The stronger galaxy–filament alignment we find among galaxies matched with filaments with lower inclinations could be in part related to how well the orientation of filaments in three dimensions is defined observationally. It is more likely that filaments with smaller inclinations will have their orientation more accurately defined, as (i) we are more precise in determining the RA and Dec. of filaments compared to the spectroscopic redshifts and (ii) there is inevitable ambiguity in determining the true distance due to the peculiar velocities of galaxies. On the other hand, the absence of galaxy–filament alignment among low-ellipticity galaxies could be partly due to the increased uncertainty in optical position angle measurements with decreasing optical ellipticity (see Section 2.2).

Although we have confirmed a statistically significant alignment signal between galaxies and filaments, it is worth pointing out that there is a high level of randomness in the galaxy–filament angle distribution. This indicates that processes that randomize the filament–galaxy angle are common even in the cosmic filament environment. One example of such processes is mergers that do not occur along the direction of filaments. If there was a relatively recent merger event that produced stellar shells and streams, it can affect the optical position angle measurements. The tidal debris can live for several billion years before it disperses and settles into the gravitational potential of the central galaxies (Quinn 1984; Hendel & Johnston 2015; Pop et al. 2018).

4.1.2 *Mechanisms for jet–optical galaxy alignment*

All extended radio jets in our sample are produced by the SMBH at the centre of galaxies. The direction of radio jets powered by the accreting material is expected to align with the spin axes of the black hole, which is affected by the angular momentum of gas in the inner accretion disc (Bardeen & Petterson 1975). If gas accreting on to the black hole has a comparable angular momentum with galactic gas at larger scales, the direction of jets would be aligned with the angular momentum of the host galaxy ('secular accretion'). However, the angular momentum of gas related to individual accretion events is not always equivalent to that of larger scale gas motion (King & Pringle 2007). Mergers and secular gas disc instabilities can generate large-scale perturbations that lead to chaotic accretion of gas on to black holes (Hobbs et al. 2011; Hopkins et al. 2012). Using numerical simulations, Peirani et al. (2024) show that the alignment between black hole spin and galaxy angular momentum depends on various factors, such as stellar mass and kinematic morphology.

In Section 3.2, we find that radio jets of our sample galaxies are overall perpendicular to the optical major axis (see Fig. 10). This result suggests that secular accretion is in action. This is in line with previous observational studies by Battye & Browne (2009), Zheng et al. (2024), and Fernández Gil et al. (2024). However, we also confirm that there is a notable level of randomness in the jet–galaxy angle distribution. Specifically, the randomness is higher among galaxies closer than $\approx$8 Mpc to the nearest cosmic filaments. As

discussed in the previous section, galaxies in our sample are likely to have experienced numerous mergers while travelling along cosmic filaments. The angular momentum of nuclear gas accreting on to the black hole, as well as the black hole spin itself (Peirani et al. 2024), can be significantly disturbed by galaxy–galaxy interactions. This leads to more chaotic accretion that produces randomly oriented jets with respect to the galactic stellar and gas distribution.

4.2 Implication

4.2.1 Absence of large-scale alignment of radio jets

In recent years, there has been an ongoing search for coherent orientation of radio jets over a large area of the sky to test the influence of large-scale cosmic environment on the evolution of galaxies and accretion of gas on to the SMBH. However, the results are contentious (Taylor & Jagannathan 2016; Contigiani et al. 2017; Osinga et al. 2020; Panwar et al. 2020; Mandarakas et al. 2021; Simonte et al. 2023).

We have shown in this paper that (i) the major axis of galaxies tends to align with the closest cosmic filament if a galaxy is closer than $\lesssim$11 Mpc from the filaments and (ii) radio jets are generally perpendicular to the major axis of the galaxy. Therefore, any putative large-scale alignment among observed radio jets can be attributed to the combined effect of these two. However, when more carefully considering the environment galaxies reside in, we find that the preference towards jets aligning perpendicular to the galaxy's major axis weakens in environments close to filaments ($\lesssim$8 Mpc). The physical mechanisms behind this are discussed in Section 4.1. Combining these results together, we argue that it is hard to expect a strong large-scale alignment of radio jets caused by cosmic filaments.

4.2.2 Intrinsic alignment of galaxies

Weak lensing quantifies the correlation between observed galaxy shape distortions, i.e. cosmic shear, to infer the mass distribution of the Universe. It is one of the key science projects for ongoing and upcoming large observing programmes, such as the Dark Energy Survey (DES; Abbott et al. 2021), the Vera Rubin Observatory (Ivezić et al. 2019), and *Euclid* (Laureijs et al. 2011; Amendola et al. 2018; Euclid Collaboration 2024). Under the assumption that the Universe is homogeneous and isotropic, the orientation of galaxies is expected to be random before the light is lensed.

However, a non-negligible correlation between galaxy ellipticities, i.e. the intrinsic alignment of galaxies, indeed affects weak lensing cosmic shear measurements. Previous studies have shown that the intrinsic alignment between galaxies is stronger for bright galaxies (Hirata et al. 2007; Joachimi et al. 2011; Singh et al. 2015). In Section 3.1, we show that radio galaxies with stellar mass $>10^{11}$ $M_{\odot}$ tend to align with the closest cosmic filament. This is direct evidence that cosmic filaments are at least in part responsible for imposing a locally preferred orientation on galaxies. Though we do not aim to quantify the pairwise alignment between galaxies in this work, our results highlight the importance of accounting for intrinsic alignment to accurately interpret cosmological weak lensing surveys (Croft & Metzler 2000; Heavens, Refregier & Heymans 2000).

Furthermore, many studies have shown that feedback from AGN, and specifically mechanical feedback from jets at $z < 1$, can disrupt the mass distribution within the dark matter halo (e.g. Peirani et al. 2017; Chisari et al. 2018; Foreman et al. 2020). Our work suggests that the impact of jets, in galaxies that are most aligned with the large-scale filamentary structures, will also preferentially deposit energy along the minor axis of the dark matter halo that is tidally aligned with the large-scale structure. This would suggest that accurately incorporating AGN feedback effects on small scales in cosmological analyses will depend strongly on whether the galaxies are lying within a filament or not.

4.2.3 Azimuthal anisotropy within the boundary of galactic haloes

Many spectral line studies on diffuse gas suggest that the observed distribution of the multiphase circumgalactic medium (CGM) around galaxies is not azimuthally isotropic (e.g. Bordoloi et al. 2011; Bouché et al. 2012; Kacprzak, Churchill & Nielsen 2012; Kacprzak et al. 2015; Huang et al. 2016). Specifically, some studies along this line focus on massive galaxy populations (Zhang et al. 2018; Zhang & Zaritsky 2022) and suggest that the inner CGM of these systems, especially along the direction of the galaxy minor axis, is ionized by radiation from AGN activities. Such asymmetries in the CGM properties are predicted by cosmological hydrodynamic simulations (e.g. Péroux et al. 2020; Nelson et al. 2021; Pillepich et al. 2021; Truong et al. 2021; Ramesh et al. 2023) and are often attributed to the result of bipolar outflow along the minor axis of galaxies, either or both from the AGN and stellar feedback, and cold inflow along the major axis of galaxies.

According to the analytical calculation by Rawlings & Jarvis (2004), the amount of energy injected by radio-mode AGN feedback is powerful enough to gravitationally unbind the CGM of the AGN host galaxy as well as its neighbouring satellite galaxies. Based on our finding that radio jets tend to align with the optical minor axis of galaxies in a statistically large sample, we support the scenario that radio-mode AGN feedback is one of the mechanisms shaping the anisotropy in the CGM around massive radio galaxies. However, we suggest that such an AGN contribution could depend on the cosmic environment since we observe that the direction of radio jets becomes more random with respect to the orientation of the optical host galaxy the closer it gets to cosmic filaments. On the other hand, we find that the optical major axis of galaxies is preferentially aligned with the direction of the cosmic filaments they reside within. This trend suggests that the accretion of matter on to these galaxies brought by cosmic filaments is directed along the galactic major axis and supports the scenario that the cold accretion of the IGM could be responsible for the anisotropy of the CGM.

Azimuthal anisotropy is found not only in CGM properties but also in satellite galaxy populations in galaxy clusters. A number of recent studies demonstrated that there is an excess of star-forming, blue satellite galaxy population along the minor axis of the brightest cluster galaxies (BCGs) compared to the major axis (Huang et al. 2016; Martín-Navarro et al. 2021; Stott 2022; Ando, Shimasaku & Ito 2023; Karp, Lange & Wechsler 2023; Stephenson et al. 2025). Several physical mechanisms have been proposed to explain this trend. First, Martín-Navarro et al. (2021) suggest that satellite galaxies could experience weaker ram pressure along the minor axis where AGN outflows take place. As mentioned in the previous paragraph, our results showing the alignment of radio jets with galaxy minor axes support this picture that AGN feedback, at least to some degree, contributes to shaping the anisotropic CGM structure that could lead to the differential ram pressure stripping along different axes. On the other hand, Stott (2022) suggests an alternative scenario in which the elongated shape of the clusters itself causes the differential ram pressure stripping towards the major and minor axes. Furthermore, recent work by Stephenson et al. (2025) shows that the excessive population of quenched galaxies

along the BCG major axis extends out to several virial radii of the clusters in their sample. They explain this to be a combined outcome of (i) satellite galaxies undergoing quenching in cosmic filaments before falling into clusters and (ii) the BCG major axis aligning with the large-scale structure (see also theoretical works by Karp et al. 2023; Zakharova et al. 2025). Though in this work we do not address the former, which is often referred to as pre-processing, there is ample evidence that cosmic filaments do affect the star formation of galaxies (Sarron et al. 2019; Hoosain et al. 2024) and a significant fraction of satellite systems in clusters assemble through this channel (Han et al. 2018; Jung et al. 2018; Kuchner et al. 2022). As for the second point, we have shown that the optical major axis of massive galaxies in cosmic filament environments tends to align with the direction of the nearest filament. Therefore, we support the proposition that the azimuthal segregation of satellite galaxies based on their star formation status can be a natural outcome of the hierarchical formation of the large-scale structure of the Universe.

5 SUMMARY

In this paper, we analyse the position angles of the optical and radio major axes and the orientation of filaments closest to galaxies. We use DESI Legacy Imaging Surveys for the optical data, LoTSS DR2 radio-optical cross-matching catalogue for the radio data, and the DisPerSE filament finder algorithm on SDSS DR12 galaxy distribution for the filament catalogue. All galaxies used in this study are radio galaxies with stellar mass above $M_* > 10^{11}\,\mathrm{M}_\odot$. For the analysis of radio jet position angles, we select a subsample with bright extended radio sources. The distance between galaxies and filaments is measured in 3D. The position angles are compared in the projected sky plane, and we apply the parallel transport method wherever appropriate.

Here are the main findings of this paper.

(i) In the cosmic filament environment, more specifically, within $\lesssim$11 Mpc of filaments, a galaxy's major axis tends to align with the orientation of the closest filament. This galaxy–filament alignment is more robust in the regions closer to the filament spine and is affected by the projection effect.

(ii) Radio jets are, in general, aligned perpendicularly to the major axis of their host galaxy. However, within $\lesssim$8 Mpc from cosmic filaments, jets are more randomly oriented with respect to the optical major axis.

These results have three major implications. First, massive galaxies in the cosmic filament environment grow by directional merger along the filaments they reside in. We expect the impact parameter of cosmic filaments in this regard to be $\lesssim$11 Mpc. Mergers along filaments lead to the large-scale elongation of the dark matter halo and stellar distribution, resulting in the alignment of the optical major axis and the filament orientation. The spin axis of the SMBH is more easily affected by individual merger events, and the chaotic accretion on to the black hole produces randomly directed jets.

Secondly, cosmic filaments could be responsible for the large-scale alignment of radio jets if there is any. The search for the alignment among adjacent jets has been a topic of interest with the rise of large-area radio surveys as a test for the connection between cosmic large-scale environments and the growth of SMBH. However, we demonstrate that the effect of cosmic filaments on the SMBH feedback manifests itself in the more randomized angle between jets and their host galaxies. Therefore, we expect the alignment signal to be extremely weak due to environmental effects on jet orientation.

Finally, the alignment of radio jets with the optical minor axis suggests that radio-mode AGN feedback could be one of the mechanisms driving the observed azimuthal anisotropy distribution of the CGM. Meanwhile, the alignment of the optical major axis with the filament orientation is related to the hierarchical assembly of clusters within the large-scale structure. Both mechanisms have been suggested to explain the observed azimuthal segregation of satellite galaxies in galaxy clusters based on their star formation status, though they are likely to work at different radii.

ACKNOWLEDGEMENTS

We thank the anonymous reviewer for constructive feedback, which significantly improved the paper. SLJ, MJJ, MNT, and TY acknowledge the support of a UKRI Frontiers Research Grant (EP/X026639/1), which was selected by the European Research Council, and the STFC consolidated grants (ST/S000488/1 and ST/W000903/1). IHW, MJJ, CLH, and MNT also acknowledge support from the Oxford Hintze Centre for Astrophysical Surveys, which is funded through generous support from the Hintze Family Charitable Foundation.

Our analysis was performed using the PYTHON programming language (Python Software Foundation; https://www.python.org). The following packages were used throughout the analysis: NUMPY (Harris et al. 2020), SCIPY (Virtanen et al. 2020), and MATPLOTLIB (Hunter 2007). This work also made use of ASTROPY[6]: a community-developed core PYTHON package and an ecosystem of tools and resources for astronomy (Astropy Collaboration 2013, 2018, 2022).

LoTSS DR 2 data products were provided by the LOFAR Surveys Key Science project (LSKSP; https://lofar-surveys.org/) and were derived from observations with the International LOFAR Telescope (ILT). LOFAR (van Haarlem et al. 2013) is the Low Frequency Array designed and constructed by ASTRON. It has observing, data processing, and data storage facilities in several countries, which are owned by various parties (each with their own funding sources), and which are collectively operated by the ILT foundation under a joint scientific policy. The efforts of the LSKSP have benefited from funding from the European Research Council, NOVA, NWO, CNRS-INSU, the SURF Co-operative, the UK Science and Technology Funding Council, and the Jülich Supercomputing Centre.

The Legacy Surveys consist of three individual and complementary projects: the DECaLS (Proposal ID #2014B-0404; PIs: David Schlegel and Arjun Dey), the BASS (NOAO Proposal ID #2015A-0801; PIs: Zhou Xu and Xiaohui Fan), and the MzLS (Proposal ID #2016A-0453; PI: Arjun Dey). DECaLS, BASS, and MzLS together include data obtained, respectively, at the Blanco telescope, Cerro Tololo Inter-American Observatory, NSF's NOIRLab; the Bok telescope, Steward Observatory, University of Arizona; and the Mayall telescope, Kitt Peak National Observatory, NOIRLab. Pipeline processing and analyses of the data were supported by NOIRLab and the Lawrence Berkeley National Laboratory (LBNL). The Legacy Surveys project is honoured to be permitted to conduct astronomical research on Iolkam Du'ag (Kitt Peak), a mountain with particular significance to the Tohono O'odham Nation.

NOIRLab is operated by the Association of Universities for Research in Astronomy (AURA) under a cooperative agreement with the National Science Foundation. LBNL is managed by the Regents

[6]http://www.astropy.org

of the University of California under contract to the U.S. Department of Energy.

This project used data obtained with the DECam, which was constructed by the Dark Energy Survey (DES) collaboration. Funding for the DES Projects has been provided by the U.S. Department of Energy, the U.S. National Science Foundation, the Ministry of Science and Education of Spain, the Science and Technology Facilities Council of the United Kingdom, the Higher Education Funding Council for England, the National Center for Supercomputing Applications at the University of Illinois at Urbana-Champaign, the Kavli Institute of Cosmological Physics at the University of Chicago, Center for Cosmology and Astro-Particle Physics at the Ohio State University, the Mitchell Institute for Fundamental Physics and Astronomy at Texas A&M University, Financiadora de Estudos e Projetos, Fundacao Carlos Chagas Filho de Amparo, Financiadora de Estudos e Projetos, Fundacao Carlos Chagas Filho de Amparo a Pesquisa do Estado do Rio de Janeiro, Conselho Nacional de Desenvolvimento Cientifico e Tecnologico and the Ministerio da Ciencia, Tecnologia e Inovacao, the Deutsche Forschungsgemeinschaft, and the Collaborating Institutions in the DES. The Collaborating Institutions are Argonne National Laboratory, the University of California at Santa Cruz, the University of Cambridge, Centro de Investigaciones Energeticas, Medioambientales y Tecnologicas-Madrid, the University of Chicago, University College London, the DES-Brazil Consortium, the University of Edinburgh, the Eidgenossische Technische Hochschule (ETH) Zurich, Fermi National Accelerator Laboratory, the University of Illinois at Urbana-Champaign, the Institut de Ciencies de l'Espai (IEEC/CSIC), the Institut de Fisica d'Altes Energies, Lawrence Berkeley National Laboratory, the Ludwig Maximilians Universitat Munchen and the associated Excellence Cluster Universe, the University of Michigan, NSF's NOIRLab, the University of Nottingham, the Ohio State University, the University of Pennsylvania, the University of Portsmouth, SLAC National Accelerator Laboratory, Stanford University, the University of Sussex, and Texas A&M University.

BASS is a key project of the Telescope Access Program (TAP), which has been funded by the National Astronomical Observatories of China, the Chinese Academy of Sciences (the Strategic Priority Research Program 'The Emergence of Cosmological Structures' Grant # XDB09000000), and the Special Fund for Astronomy from the Ministry of Finance. The BASS is also supported by the External Cooperation Program of Chinese Academy of Sciences (Grant # 114A11KYSB20160057), and Chinese National Natural Science Foundation (Grant # 12120101003, # 11433005).

The Legacy Survey team makes use of data products from the Near-Earth Object Wide-field Infrared Survey Explorer (NEOWISE), which is a project of the Jet Propulsion Laboratory/California Institute of Technology. NEOWISE is funded by the National Aeronautics and Space Administration.

The Legacy Surveys imaging of the DESI footprint is supported by the Director, Office of Science, Office of High Energy Physics of the U.S. Department of Energy under Contract No. DE-AC02-05CH1123, by the National Energy Research Scientific Computing Center, a Department of Energy Office of Science User Facility under the same contract, and by the U.S. National Science Foundation, Division of Astronomical Sciences under Contract No. AST-0950945 to NOAO.

This work makes use of the service L3S/COSFIL, the Large Scale Structure Services developed by Observatoires des Sciences de l'Univers Paris Saclay (OSUPS), Observatoire de la Côte d'Azur (OCA), Pytheas, and the Baryon Picture of the Cosmos (ByoPiC) products.

DATA AVAILABILITY

LoTSS DR2 radio-optical cross-match catalogue (Hardcastle et al. 2023) is publicly available at https://lofar-surveys.org/dr2_release.html. Data product of the DESI Legacy Imaging Surveys (Dey et al. 2019) is available at https://www.legacysurvey.org/. The Galaxy Zoo DESI morphology classification catalogue (Walmsley et al. 2023) is available at https://zenodo.org/records/8360385. The catalogue of SDSS cosmic filaments (Malavasi et al. 2020) can be downloaded at https://l3s.osups.universite-paris-saclay.fr/cosfil.html.

REFERENCES

Abbott T. M. C. et al., 2021, ApJS, 255, 20
Adams N. J., Bowler R. A. A., Jarvis M. J., Häußler B., Lagos C. D. P., 2021, MNRAS, 506, 4933
Ahumada R. et al., 2020, ApJS, 249, 3
Aihara H. et al., 2011, ApJS, 193, 29
Alam S. et al., 2015, ApJS, 219, 12
Allgood B., Flores R. A., Primack J. R., Kravtsov A. V., Wechsler R. H., Faltenbacher A., Bullock J. S., 2006, MNRAS, 367, 1781
Amendola L. et al., 2018, Living Rev. Relativ., 21, 2
Ando M., Shimasaku K., Ito K., 2023, MNRAS, 519, 13
Aragón-Calvo M. A., van de Weygaert R., Jones B. J. T., van der Hulst J. M., 2007, ApJ, 655, L5
Astropy Collaboration, 2013, A&A, 558, A33
Astropy Collaboration, 2018, AJ, 156, 123
Astropy Collaboration, 2022, ApJ, 935, 167
Bardeen J. M., Petterson J. A., 1975, ApJ, 195, L65
Barsanti S. et al., 2022, MNRAS, 516, 3569
Barsanti S. et al., 2023, MNRAS, 526, 1613
Battye R. A., Browne I. W. A., 2009, MNRAS, 399, 1888
Best P. N., Heckman T. M., 2012, MNRAS, 421, 1569
Bett P., Eke V., Frenk C. S., Jenkins A., Helly J., Navarro J., 2007, MNRAS, 376, 215
Binney J., 1978, MNRAS, 183, 501
Binney J., Tremaine S., 2008, Galactic Dynamics, 2nd edn. Princeton Univ. Press, Princeton, NJ
Birkinshaw M., Davies R. L., 1985, ApJ, 291, 32
Bond N. A., Strauss M. A., Cen R., 2010, MNRAS, 409, 156
Bonjean V., Aghanim N., Douspis M., Malavasi N., Tanimura H., 2020, A&A, 638, A75
Bordoloi R. et al., 2011, ApJ, 743, 10
Bouché N., Hohensee W., Vargas R., Kacprzak G. G., Martin C. L., Cooke J., Churchill C. W., 2012, MNRAS, 426, 801
Bower R. G., Benson A. J., Malbon R., Helly J. C., Frenk C. S., Baugh C. M., Cole S., Lacey C. G., 2006, MNRAS, 370, 645
Bower R. G., Schaye J., Frenk C. S., Theuns T., Schaller M., Crain R. A., McAlpine S., 2017, MNRAS, 465, 32
Bridle S. et al., 2009, Ann. Appl. Stat., 3, 6
Cautun M., van de Weygaert R., Jones B. J. T., Frenk C. S., 2014, MNRAS, 441, 2923
Chisari N. et al., 2015, MNRAS, 454, 2736
Chisari N. E. et al., 2018, MNRAS, 480, 3962
Codis S., Pichon C., Devriendt J., Slyz A., Pogosyan D., Dubois Y., Sousbie T., 2012, MNRAS, 427, 3320
Contigiani O. et al., 2017, MNRAS, 472, 636
Croft R. A. C., Metzler C. A., 2000, ApJ, 545, 561
Croton D. J. et al., 2006, MNRAS, 365, 11
Davé R., Anglés-Alcázar D., Narayanan D., Li Q., Rafieferantsoa M. H., Appleby S., 2019, MNRAS, 486, 2827
DESI Collaboration, 2024, AJ, 168, 58
Dey A. et al., 2019, AJ, 157, 168
Dubois Y. et al., 2014, MNRAS, 444, 1453
Dubois Y., Peirani S., Pichon C., Devriendt J., Gavazzi R., Welker C., Volonteri M., 2016, MNRAS, 463, 3948
Emsellem E. et al., 2011, MNRAS, 414, 888

Euclid Collaboration, 2024, preprint (arXiv:2405.13491)
Fabian A. C., 2012, ARA&A, 50, 455
Fernández Gil D. et al., 2024, Nat. Astron., 9, 302
Foreman S., Coulton W., Villaescusa-Navarro F., Barreira A., 2020, MNRAS, 498, 2887
Galárraga-Espinosa D., Aghanim N., Langer M., Gouin C., Malavasi N., 2020, A&A, 641, A173
Han S., Smith R., Choi H., Cortese L., Catinella B., Contini E., Yi S. K., 2018, ApJ, 866, 78
Hardcastle M. J. et al., 2023, A&A, 678, A151
Harris C. R. et al., 2020, Nature, 585, 357
Hatch N. A. et al., 2014, MNRAS, 445, 280
Heavens A., Refregier A., Heymans C., 2000, MNRAS, 319, 649
Heckman T. M., Best P. N., 2014, ARA&A, 52, 589
Heckman T. M., Roy N., Best P. N., Kondapally R., 2024, ApJ, 977, 125
Hendel D., Johnston K. V., 2015, MNRAS, 454, 2472
Herbert P. D., Jarvis M. J., Willott C. J., McLure R. J., Mitchell E., Rawlings S., Hill G. J., Dunlop J. S., 2011, MNRAS, 410, 1360
Hirata C. M., Mandelbaum R., Ishak M., Seljak U., Nichol R., Pimbblet K. A., Ross N. P., Wake D., 2007, MNRAS, 381, 1197
Hirv A., Pelt J., Saar E., Tago E., Tamm A., Tempel E., Einasto M., 2017, A&A, 599, A31
Hobbs A., Nayakshin S., Power C., King A., 2011, MNRAS, 413, 2633
Hoosain M. et al., 2024, MNRAS, 528, 4139
Hopkins P. F., Hernquist L., Hayward C. C., Narayanan D., 2012, MNRAS, 425, 1121
Huang Y.-H., Chen H.-W., Johnson S. D., Weiner B. J., 2016, MNRAS, 455, 1713
Hunter J. D., 2007, Comput. Sci. Eng., 9, 90
Ivezić Ž. et al., 2019, ApJ, 873, 111
Jain P., Narain G., Sarala S., 2004, MNRAS, 347, 394
Jarvis M. J., Rawlings S., Eales S., Blundell K. M., Bunker A. J., Croft S., McLure R. J., Willott C. J., 2001, MNRAS, 326, 1585
Joachimi B., Mandelbaum R., Abdalla F. B., Bridle S. L., 2011, A&A, 527, A26
Jung S. L., Choi H., Wong O. I., Kimm T., Chung A., Yi S. K., 2018, ApJ, 865, 156
Jung S. L. et al., 2022, MNRAS, 515, 22
Kacprzak G. G., Churchill C. W., Nielsen N. M., 2012, ApJ, 760, L7
Kacprzak G. G., Muzahid S., Churchill C. W., Nielsen N. M., Charlton J. C., 2015, ApJ, 815, 22
Kang X., Wang P., 2015, ApJ, 813, 6
Karp J. S. M., Lange J. U., Wechsler R. H., 2023, ApJ, 949, L13
King A. R., Pringle J. E., 2007, MNRAS, 377, L25
Kormendy J., Richstone D., 1995, ARA&A, 33, 581
Kraljic K., Duckworth C., Tojeiro R., Alam S., Bizyaev D., Weijmans A.-M., Boardman N. F., Lane R. R., 2021, MNRAS, 504, 4626
Kuchner U. et al., 2022, MNRAS, 510, 581
Lang D., Hogg D. W., Schlegel D. J., 2016, AJ, 151, 36
Laureijs R. et al., 2011, preprint (arXiv:1110.3193)
Lee J., Erdogdu P., 2007, ApJ, 671, 1248
Lee J., Moon J.-S., 2023, ApJ, 951, L26
Lee J., Springel V., Pen U.-L., Lemson G., 2008, MNRAS, 389, 1266
Libeskind N. I., Hoffman Y., Forero-Romero J., Gottlöber S., Knebe A., Steinmetz M., Klypin A., 2013, MNRAS, 428, 2489
Libeskind N. I., Knebe A., Hoffman Y., Gottlöber S., 2014, MNRAS, 443, 1274
McAlpine K., Smith D. J. B., Jarvis M. J., Bonfield D. G., Fleuren S., 2012, MNRAS, 423, 132
Mackay C. D., 1971, MNRAS, 151, 421
McLeod D. J., McLure R. J., Dunlop J. S., Cullen F., Carnall A. C., Duncan K., 2021, MNRAS, 503, 4413
McLure R. J., Jarvis M. J., 2004, MNRAS, 353, L45
McNamara B. R., Nulsen P. E. J., 2012, New J. Phys., 14, 055023
Malavasi N., Aghanim N., Douspis M., Tanimura H., Bonjean V., 2020, A&A, 642, A19
Mandarakas N., Blinov D., Casadio C., Pelgrims V., Kiehlmann S., Pavlidou V., Tassis K., 2021, A&A, 653, A123
Martín-Navarro I., Pillepich A., Nelson D., Rodriguez-Gomez V., Donnari M., Hernquist L., Springel V., 2021, Nature, 594, 187
Mentuch Cooper E. et al., 2023, ApJ, 943, 177
Mingo B., Hardcastle M. J., Croston J. H., Dicken D., Evans D. A., Morganti R., Tadhunter C., 2014, MNRAS, 440, 269
Mohan N., Rafferty D., 2015, Astrophysics Source Code Library, record ascl:1502.007
Morinaga Y., Ishiyama T., 2020, MNRAS, 495, 502
Nelson D., Byrohl C., Peroux C., Rubin K. H. R., Burchett J. N., 2021, MNRAS, 507, 4445
Osinga E. et al., 2020, A&A, 642, A70
Palimaka J. J., Bridle A. H., Fomalont E. B., Brandie G. W., 1979, ApJ, 231, L7
Panwar M., Prabhakar, Sandhu P. K., Wadadekar Y., Jain P., 2020, MNRAS, 499, 1226
Peirani S. et al., 2017, MNRAS, 472, 2153
Peirani S. et al., 2024, A&A, 686, A233
Péroux C., Nelson D., van de Voort F., Pillepich A., Marinacci F., Vogelsberger M., Hernquist L., 2020, MNRAS, 499, 2462
Pillepich A., Nelson D., Truong N., Weinberger R., Martin-Navarro I., Springel V., Faber S. M., Hernquist L., 2021, MNRAS, 508, 4667
Planck Collaboration XIII, 2016, A&A, 594, A13
Pop A.-R., Pillepich A., Amorisco N. C., Hernquist L., 2018, MNRAS, 480, 1715
Quinn P. J., 1984, ApJ, 279, 596
Ramesh R., Nelson D., Heesen V., Brüggen M., 2023, MNRAS, 526, 5483
Rawlings S., Jarvis M. J., 2004, MNRAS, 355, L9
Reid B. et al., 2016, MNRAS, 455, 1553
Sansom A. E. et al., 1987, MNRAS, 229, 15
Sarron F., Adami C., Durret F., Laigle C., 2019, A&A, 632, A49
Schaye J. et al., 2015, MNRAS, 446, 521
Shimwell T. W. et al., 2019, A&A, 622, A1
Shimwell T. W. et al., 2022, A&A, 659, A1
Simonte M., Andernach H., Brüggen M., Best P. N., Osinga E., 2023, A&A, 672, A178
Singh S., Mandelbaum R., More S., 2015, MNRAS, 450, 2195
Smith D. J. B. et al., 2016, in Reylé C., Richard J., Cambrésy L., Deleuil M., Pécontal E., Tresse L., Vauglin I., eds, SF2A-2016: Proceedings of the Annual Meeting of the French Society of Astronomy and Astrophysics, p. 271 , preprint (arXiv:1611.02706)
Sousbie T., 2011, MNRAS, 414, 350
Springel V. et al., 2005, Nat. Astrophys., 435, 629
Stephenson H., Stott J., Butler J., Webster M., Head J., 2025, MNRAS, 537, 1542
Stott J. P., 2022, MNRAS, 511, 2659
Strauss M. A. et al., 2002, AJ, 124, 1810
Sutherland W., Saunders W., 1992, MNRAS, 259, 413
Taylor A. R., Jagannathan P., 2016, MNRAS, 459, L36
Tempel E., Libeskind N. I., 2013, ApJ, 775, L42
Tempel E., Tago E., Liivamägi L. J., 2012, A&A, 540, A106
Tenneti A., Mandelbaum R., Di Matteo T., Feng Y., Khandai N., 2014, MNRAS, 441, 470
Trowland H. E., Lewis G. F., Bland-Hawthorn J., 2013, ApJ, 762, 72
Truong N., Pillepich A., Nelson D., Werner N., Hernquist L., 2021, MNRAS, 508, 1563
Tudorache M. N. et al., 2022, MNRAS, 513, 2168
Urry C. M., Padovani P., 1995, PASP, 107, 803
Valtonen M. J., 1983, Ap&SS, 90, 207
van de Sande J. et al., 2017, MNRAS, 472, 1272
van Haarlem M. P. et al., 2013, A&A, 556, A2
Veale M. et al., 2017, MNRAS, 464, 356
Vera-Ciro C. A., Sales L. V., Helmi A., Frenk C. S., Navarro J. F., Springel V., Vogelsberger M., White S. D. M., 2011, MNRAS, 416, 1377
Virtanen P. et al., 2020, Nat. Methods, 17, 261
Walmsley M. et al., 2023, MNRAS, 526, 4768
Wang P., Kang X., 2017, MNRAS, 468, L123
Wang W. et al., 2024, MNRAS, 532, 4604

Whittam I. H., Prescott M., McAlpine K., Jarvis M. J., Heywood I., 2018, MNRAS, 480, 358
Whittam I. H. et al., 2022, MNRAS, 516, 245
Williams W. L. et al., 2019, A&A, 622, A2
Zakharova D., McGee S., Vulcani B., De Lucia G., 2025, A&A, 693, A113
Zhang H., Zaritsky D., 2022, ApJ, 941, 18
Zhang Y., Yang X., Faltenbacher A., Springel V., Lin W., Wang H., 2009, ApJ, 706, 747
Zhang Y., Yang X., Wang H., Wang L., Luo W., Mo H. J., van den Bosch F. C., 2015, ApJ, 798, 17
Zhang H., Zaritsky D., Werk J., Behroozi P., 2018, ApJ, 866, L4
Zheng X., Zhang Y., Röttgering H., 2024, A&A, 686, A169
Zou H. et al., 2017, PASP, 129, 064101

This paper has been typeset from a TEX/LATEX file prepared by the author.